On the affine skeleton of 3D models of the human body

by Vasileios Zografos

2003

Supervisor: Prof. Bernard Buxton

This report is submitted as part requirement for the MRes Degree in Computer Vision, Image Processing, Graphics and Simulation at University College London. It is substantially the result of my own work except where explicitly indicated in the text.

ABSTRACT

The skeleton of a shape in 2d or object in 3d, is a simplified representation of that shape or object. It has been the focus of research in many different fields and has found a variety of application areas, in computer graphics, machine vision, medical image processing, robotic navigation, document processing and so on. The most common skeleton is the medial axis, originally defined by Blum and has been the standard for many years. However, it has certain inherent disadvantages such as being very sensitive to boundary and volumetric noise and also not invariant under affine transformations. Recently, Betelu et al. have proposed the theory and algorithm for creating the 3d affine invariant skeleton by means of 3d affine erosion. In this project, we have studied the proposed algorithm and introduced further improvements in order to build the software for affine erosion of 3d objects. We have used this software in a number of 3d primitives but more importantly in 3d models of the human body, and compared the results with common 3d skeletonisation methods. We examined whether this skeleton fulfils the requirements for noise resistance and affine invariance, and went on to discuss some possible application areas for this type of skeleton. We identified the limitations of this algorithm and proposed some ideas on how it can be further improved in the future.

CONTENTS

1 INTRODUCTION

This chapter begins with a brief background introduction on the skeleton of a shape (or object in 3D), some of the most common skeletonisation methods and popular application areas. It then goes on to describe the main problems associated with using a skeleton in computer graphics and how this project aims to contribute towards the solution of some of these shortcomings. Any such contributions and advances are briefly described here. Finally, this chapter concludes with the structure and content of the report.

1.1 BACKGROUND

Starting with the definition of the skeleton, it can be said that a skeleton of a shape in two dimensions, or of an object in three, is simply the result of a skeletonisation process on this shape or object. Such a skeletonisation process is one where discrete sample points are gradually removed from the object or shape, while preserving its *continuity* and *connectivity*, in order to generate a more simple representation of the object or shape. There are of course alternative definitions for the skeleton and as a result different kinds of skeletons. However, the general effects are similar as are the uses to which skeletons are put. Figure 1.1 shows a typical example of the skeleton (medial axis) of a rectangle.

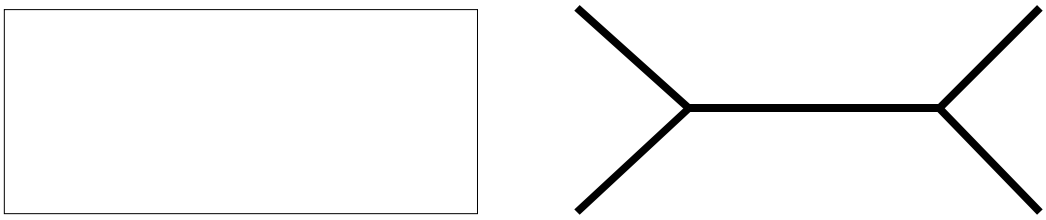

Figure 1.1 A rectangle (left) and its medial axis (right)

A skeleton therefore is a lower dimensional shape description of an object that represents the local symmetries and the topological structure of the object. There are many skeletonisation techniques, but they can be broadly organised into three classes, *thinning*, *Voronoi skeletons* and *distance transforms*.

Thinning, or morphological erosion, are methods based on Blum's grass-fire formulation [Blu64], [Blu73], and operate by successively eroding points from the boundary of the object, while retaining the end points of line segments, until no more thinning is possible. When this is accomplished, what remains is an approximation to the skeleton. This class of operations are quite sensitive to the most important geometrical transformations (translation, rotation and scaling) and typically cannot localise skeletal points accurately.

Voronoi skeletons are the result of a different class of skeletonisation operations, which are based on a special property of the Voronoi diagram. More specifically, it has been shown [Sch89] that, under appropriately chosen smoothness conditions and as the sampling rate increases, the vertices of the Voronoi diagram of a set of boundary points will converge to the exact skeleton. This idea has been used successfully [Ogn93], [SPB96] in developing skeletonisation algorithms in 2D and 3D. This method can preserve the topology and accurately localise skeletal points but only if the boundary is sampled densely enough. Unfortunately, however, the practical results of Voronoi skeletonisation methods are not invariant under Euclidean transformations and can require an additional optimisation step, which in 3D can have a high computational complexity.

The final class of skeletonisation methods, the distance functions, are based on the fact that the locus of the skeletal points are coincidental with the singularities (creases or curvature discontinuities, also known as shocks) of a distance function to the boundary. An appropriate distance metric (such as Euclidean, city-block or chessboard distance) is first used to calculate the distance transform of the object. The local maxima of this distance function or the corresponding discontinuities in its derivatives are then detected, each of which indicates a skeleton point. The numerical detection of these singularities, however, is in itself a non-trivial problem. Whereas it may be possible to have good localisation of the skeleton points, ensuring homotopy with the original object is difficult.

In digital spaces only an approximation to the true skeleton can be extracted. Therefore, these approximations need to fulfil two main requirements if they are to be considered as true approximations to the skeleton. The first is topological, which is the requirement that the skeleton will retain

the topology of the original object (i.e. properties of objects which are preserved through deformations, twistings, and stretchings). The second is geometrical, which requires that the skeleton is as thin as possible, connected, in the middle of the object and invariant under the most important geometrical transformations, including rotation, translation and scaling.

Of course these requirements are not exhaustive and may differ for different application areas. For example, object recognition requires thin skeletons with primitive features in order for similarity comparisons to take place. On the other hand, skeletons with detailed geometric information are necessary for surface reconstruction applications, so that the approximation error in the reconstruction process is minimized.

There are indeed many application areas where the skeleton of an object or shape can be used. Some of them are:

- *Fast object recognition and tracking*: This is the process of determining which, if any, of a given set of objects appear in a given image or image sequence. Since the skeleton retains shape information and is a reduced representation of the original shape it can be used to match shapes/objects much faster than conventional methods, because of the fewer number of points in the skeleton. The same idea lies behind the use of feature tracking, which is actually the correlation of an extracted object from one data set to the next. See [Su03] and references therein.

- *Animation control:* Animation usually consists of three steps: modelling, deformation and rendering. The step of deformation for polygon based animation is carried out with the help of skeletons. The animator moves the skeleton which in turn causes the object to deform in the same way. See [GKS98] and [Oli03].

- *Surface reconstruction:* This is an important process in geometric modelling for generating piecewise smooth surfaces from data captured from real objects. A medial axis transform (MAT) skeleton performs well in this case because it retains all the boundary information of the original object. Therefore, by applying the inverse transformation, it is

possible to reconstruct the surface of the object. See [ACK01] and [DG03].

- *Shape abstraction:* Skeletonisation from thinning gives a set of unconnected voxels, which can then be connected into a skeleton tree. By using the distance transform values of these voxels, it is possible to construct a graph, the minimum spanning tree (MST) of which will automatically connect the voxels. The MST contains shape information, and is subject to processing by standard, well known algorithms for searching, traversal and shortest path discovery. This in itself greatly expands the use of a skeleton to several domains. See [GS98].

- *Text processing-character recognition:* This is the process of identifying machine printed and handwritten characters in an automated or a semi-automated manner. Given a character image its skeleton is extracted and then compared with a set of templates (or prototypes). See [MP90] and [AW02].

- *Automatic navigation:* By using skeletonisation, the centreline of an object can be detected quite accurately and then can be used as a path for camera navigation in computer graphics and animation, or for path navigation in robotics. If the skeleton is centred, collisions with the object boundaries are avoided. See [WDK01].

1.2 PROBLEM STATEMENT

Articulation and animation of 3d human body models, such as these produced by the Body Lines scanner [Hor95], are dependent upon an underlying skeleton, which most often requires some manual intervention from the animator. It is possible, however, to automatically produce such skeletons by using traditional image processing techniques (such as the medial axis transform) which can be extended to 3d. Alternative techniques, such as principal components analysis (PCA) may be used to detect the main limb axes and be used as a precursor to the body skeleton, with little or no intervention. For example, Oliveira and Buxton [OB01] have approximated the medial axis of a hu-

man body scan by taking horizontal slices, locating the centroid and joining these centroids to build the skeleton.

However, even though such popular techniques may produce acceptable skeletons for certain kinds of simplistic input datasets, it is soon obvious that these skeletons are not very robust. A skeleton is considered robust if it is not significantly affected by noise present in the data or small, unimportant details on the boundary of the object. Also, it should not produce any degenerate surfaces after skeletonisation, or lead to connectivity changes after mesh simplification, subdivision and re-mesh of the original triangulated data. Last but not least, it should be invariant to the most important classes of transformation, such as Euclidean and affine transforms.

To illustrate this, let us consider the medial axis of the rectangle from Figure 1.1 above and add a small bump in the boundary of the shape. The resulting skeleton can be seen in Figure 1.2. It is immediately obvious that the medial axis can be very sensitive to small changes in the shape. The medial axis is also very sensitive to noise. To illustrate this “pepper “ noise was added to the original rectangle and its skeleton was computed. As can be seen in Figure 1.3, the skeleton attempts to connect each noise point to the skeleton obtained from the noise free image.

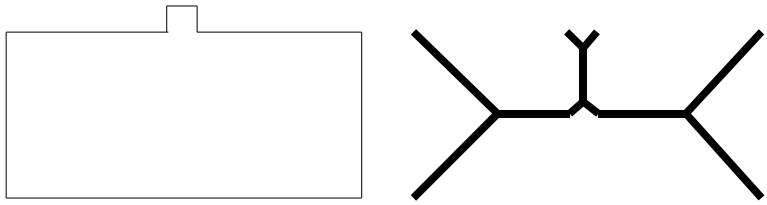

Figure 1.2 Rectangle with small bump and its skeleton

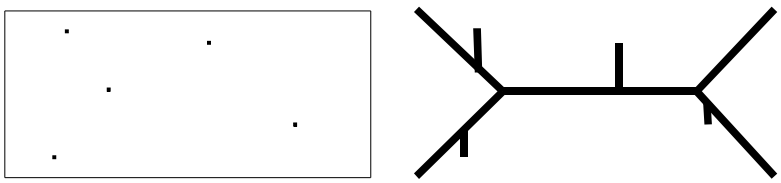

Figure 1.3 Noisy rectangle and corresponding skeleton

In addition, for more complex objects, the medial axis is not invariant under special affine trans-

formations (non-singular linear transformations composed with translations). The PCA skeleton can suffer similar noise-related effects, since spurious values in the boundary may throw off the skeletonisation process and produce limb axes that do not fall in the centre of the object. Such effects are exaggerated by the well-known sensitivity of least squares techniques, which PCA being equivalent to Pearson's regression effectively, is to outliers. To overcome such problems, it is necessary to introduce additional image processing steps (such as smoothing) before skeletonisation.

The same applies to 3d objects and in particular 3d body scans. In Figure 1.4, the medial axis of a relatively noise free human body is compared with the skeletons from the same body, but with some random surface and random volume noise added. As the illustration shows, the skeleton produced from the body scan to which surface noise has been added (the one in the middle) will reflect the surface noise with branches in the skeleton, resulting in a more complex structure. These effects are more emphasised when the noise is inside the object (volume noise), where even for a small amount of Gaussian noise the resulting skeleton can change considerably (rightmost skeleton) and even become discontinuous.
More detailed results that demonstrate the effects of noise on medial skeletons together with

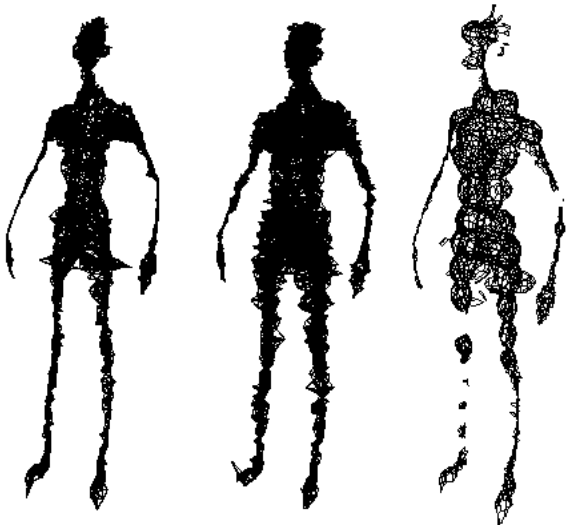

Figure 1.4 Skeleton from a body scan (left) and skeletons after addition of surface and volumetric noise the the scan (centre and right respectively).

description of how they behave under affine transformations are presented later in this report and in

the appendices.

1.3 AIM

A solution to the problems associated with the medial axis has been proposed by Betelu et al [Bet00] which produces affine invariant skeletons of 2d shapes that are not affected by noise. Recently [Bet01], this solution has been extended in 3d with promising results for simple objects although albeit quite time consuming, computationally expensive and numerically unstable process.

The primary aim of this project is to examine the application of this theory to human body scans and other objects in general, and to determine if the proposed algorithm has any benefits over existing popular and newly developed skeletonisation techniques. Part of this examination, will be to determine if and to what extent the affine invariance and noise resistance properties that worked so well in 2d, work in 3-dimensions. A secondary aim is to further improve the algorithm by reducing its running time, but also to produce an implementation that can be used with more conventional 3d formats, such as triangulated OFF files (3d data and connectivity information).

1.4 CONTRIBUTIONS

Perhaps the most significant contribution of this study on skeleton research, has been the use of the 3d affine invariant skeleton on models of the human body. So far, amongst its type of skeletons, only the medial axis has been used in body scans, which as mentioned previously is not robust nor invariant under affine transformations, unlike other one-dimensional affine invariant skeletons, a topic that will be analysed more in the next chapter.

Also, this is an important application of a theory that has been quite successful in two dimensions, but whose extension in three is not so straightforward and has not been tested thoroughly. This project attempts to test an implementation of a specific skeletonisation process (based on 3d affine erosion) with real and artificial input data and to determine whether it is indeed invariant to common transformations, how and to what extent it is affected by noise, whether it can have the potential for practical applications in object animation and how it compares with more recent advances in the area.

As far as the skeletonisation algorithm is concerned, some improvements have been implemented and others introduced, that reduce the overall running time of the skeletonisation process and perhaps the overall quality of the end result.

1.5 CONTENT AND STRUCTURE

This report is organised into seven chapters together with the bibliography and appendices.
Chapter 2 reviews the relevant literature on the subject of skeletonisation, together with any relevant background information. More specifically, the geometric concepts of the medial axis, medial surface, Voronoi skeletons and the theory behind the 3d affine invariant skeleton (based on affine erosion) is more thoroughly investigated. In addition, state of the art, alternative skeletonisation methods and their potential uses in modelling and animation are reviewed.

Chapter 3 goes a step further and describes the algorithm behind the affine invariant skeleton theory, which was presented in the previous chapter. The problems and limitations of the original algorithm are explained together with the methods proposed for their solutions and improvements to the algorithm, their impact on the running time, complexity and the overall quality of results. Computational geometry issues are also briefly included in this chapter.

In chapter 4 the software engineering aspects of the project are presented, that is, the requirements specification, analysis and design. Design or implementation problems are mentioned, and the way they were solved is discussed. Furthermore, this chapter compares the different choices for algorithms and data structures used and the way they affected the overall quality of the results. In addition, any appropriate system diagrams are included in this chapter.

Chapter 5 contains a number of software validation tests together with their results, which help establish that the software is working correctly and that the algorithms are stable and efficient with different kinds of input datasets.

Chapter 6 contains the various experiments carried out with the algorithms implemented, and the

results obtained. Both real data produced from a body scanner and artificial data where used to test the fitness of the algorithm for creating affine invariant, noise resistant skeletons. These results are then compared with the results of typical skeletonisation algorithms and appropriate conclusions are drawn.

Chapter 7 summarises the research and presents the overall conclusions. Suggestions for further research together with theoretical and algorithmic improvements to this specific approach are discussed.

Finally, we have included the appendices which contain a variety of test results and the necessary computational geometry theory, together with the planning and execution of the project and the significance of this research. The source code of this implementation has also been included.

2 LITERATURE REVIEW

Skeletons are already widely adopted in a variety of areas. Recently, application fields such as object matching [Hil01], computer animation [WP02], collision detection and mesh editing, have shown an increasing interest in the use of skeletons. In addition, because skeletons are better perceived by humans than other shape descriptions, they are best suited for human-computer interaction applications.

This chapter describes both traditionally used and recently developed skeletonisation methods, their theoretical concepts, advantages and problems, citing relevant publications as necessary. A special type of skeleton, the affine invariant skeleton, is more closely examined and the theory behind the algorithm used in this project is presented. Advances in the area of affine invariant skeletons, especially since the implementation of this project are also included as an alternative to our chosen algorithm.

2.1 TRADITIONAL SKELETONISATION METHODS

Traditionally, there are two kinds of approaches to constructing the skeleton of an object. One is to compute the skeleton directly from the object surface points, and the other to extract the skeleton by constructing a distance field of an object. Some typical examples of both of these methods are examined here.

2.1.1 DIRECT COMPUTATION METHOD

The medial axis

Perhaps the most commonly used skeleton is the medial axis, derived from Blum's original work. Empirically, the medial axis can be thought of as a branching geometric centreline of a 2d shape. In three dimensions, it becomes a centralised surface and the term medial surface is used instead. The medial axis is defined as the locus of the centres of all the maximal disks, that are inside the shape and intersect the boundary of the shape in at least two different points. Similarly, for 3d, the medial

surface is the locus of the centres of the maximal spheres. Both of these concepts can be extended to higher dimensions. Figure 2.1 shows how discrete points on the skeleton are computed via maximum inscribed circles, and also the medial surface in 3d (solid lines).

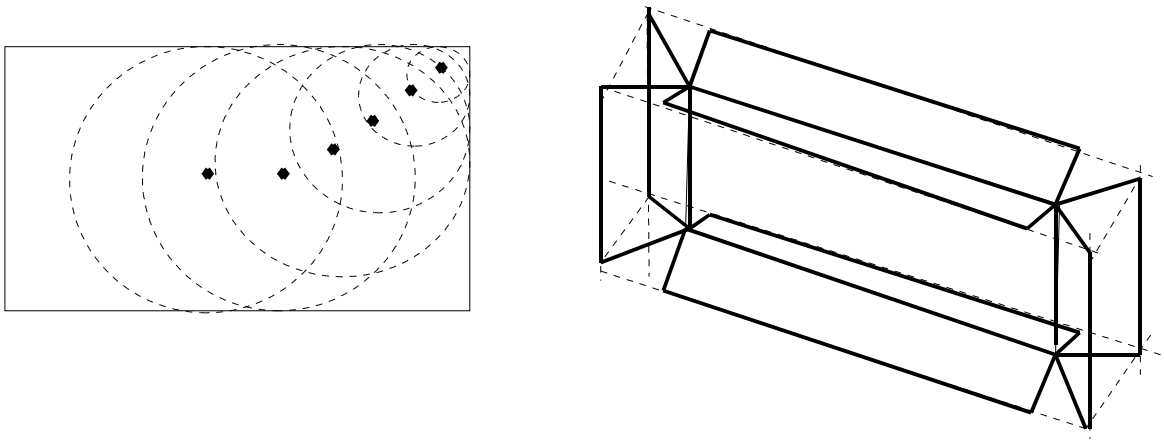

Figure 2.1 Left: Maximal circles interior to the rectangle with their centres. The centres are points on the medial axis. Right: 3d medial surface of a box

Together with the medial axis, we often store the radii of the maximal disks (or spheres). The idea behind this, is that we can use this extra information to reconstruct the original object. The medial axis in conjunction with this distance function defines the medial axis transform (MAT). The object's boundary and its MAT are equivalent, and one can be computed from the other. Usually, a 2-dimensional shape will be transformed into a 1-dimensional structure, while a 3-dimensional object will be transformed into a 2d surface.

The medial axis has been studied extensively, especially as a means for shape representation [NP85], [WOL92], object decomposition for mesh generation [She96], shape morphing and animation [Teic98] and motion planning [Wil99]. This theory however, is not without problems. We have briefly seen in the introduction, how the MAT produced undesirable skeleton branches when the curvature of the object surface varies everywhere (noisy surface). Since this is a morphologically meaningless property of the MAT, some studies have focused on the simplification of a noisy MAT by means of pruning [SB98],[Ogn95].

However, this is not the only problem with the medial axis. The medial axis is not invariant under special affine transformations (i.e. the medial axis of an affine-transformed shape is not the same as that obtained by applying the same transformation to the original medial axis). This is best illustrated in Figure 2.2, where we see the medial axis of an elliptical pie shape, akin to the examples in [JB01]. When the shape is affine-transformed, the calculated medial axis has additional branches. Clearly, it does not correspond to an affine-transform of the original axis. We will revisit the affine transform in more detail, later in this chapter.

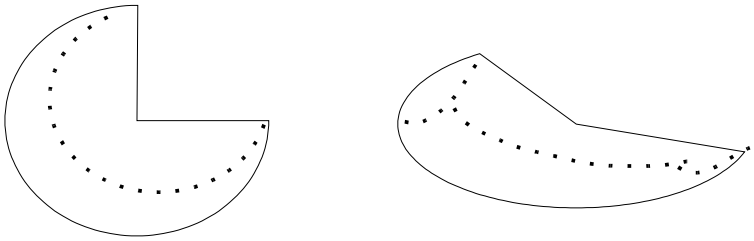

Figure 2.2 A concave curve and its medial axis, and after affine transformation

Voronoi diagram

Exact computation of the medial axis is difficult in general. Culver et al. [CKM99] and Hoffman [Hof90] have created algorithms for computing the exact medial axis for some special classes of shapes but even these algorithms had to deal with the numerical instabilities associated with the medial axis computation. An alternative method for the exact computation of the medial axis is the creation of the Voronoi diagram from the shape boundary points, and then the approximation of the MAT from that.

The Voronoi diagram is the partition of n points in a plane into n convex polygons such that each polygon contains exactly one point and every point in a given polygon is closer to the point in that polygon than to any other point (Figure 2.3). The generated polygons are known as Voronoi polygons, and from what we can see in the illustration, the points where the boundaries of these polygons meet, form an approximation to the medial axis.

Voronoi diagrams have been widely adopted in the construction of 2d and 3d skeletons [Ogn92].

More recently, Amenta et al. [ACK01], have proposed the "Power Crust" algorithm for MAT approximation and surface reconstruction, based on the idea of α-shapes (a generalisation of the convex hull). The algorithm first computes the Voronoi diagram of the scattered data points, and then retrieves a set of polar balls[1] by selecting candidates from the Voronoi balls[2] that have maximal distance to the sampled surface. After labelling these polar balls, the object described by the data points is transformed into a polar ball representation. Connecting the polar ball centres gives a good approximation to the MAT. Although this algorithm works well on dense data sets, it faces some difficulties when the data is under sampled by producing holes or other artefacts in the vicinity of the under-sampling.

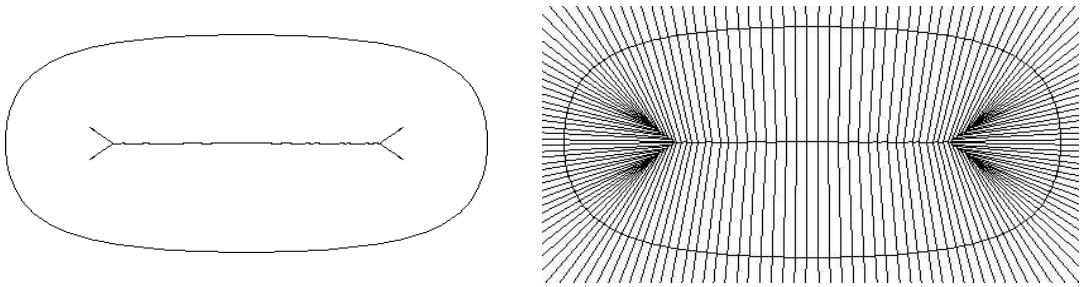

Figure 2.3 On the left a convex curve and its medial axis, and on the right the Voronoi diagram of the curve, together with its approximated medial axis.

Dey and Goswami [DG03]have created a simple algorithm called "Tight Cocone" (based on the original "Cocone" algorithm by Amenta et al. [Ame02]) for watertight surface reconstruction that can approximate the medial axis directly from the Voronoi diagram, using the algorithm by Dey and Zhao [DZ02]. Their approach does not pay any special attention to the poles (Voronoi vertices) unlike other methods, but rather computes the sub-complex from the Voronoi diagram that lies close to the medial axis and converges to it as the sampling density reaches infinity. The algorithm employs mesh simplification methods, such as sample decimation or direct medial axis simplification, to overcome the problems caused by the fact that there tend to be too many spikes in the medial axis produced by the "Power Crust" algorithm. This, together with the way that the Voronoi facets are

1 The MAT is approximated by a subset V of the Voronoi vertices of S, called the poles, which (where S is a good sample) lie near the medial axis. The balls surrounding the poles and touching the nearest samples are the polar balls.

2 The Voronoi balls for a a set S of points in R^3 , is the set B of balls centred at the Voronoi vertices of S such that $B = Vor(S)$. The polar balls are a subset of the Voronoi balls .

chosen, makes the algorithm scale and density independent and the medial axis calculation less affected by noise.

Reeb graph

A relatively up-to-date direct computation method is to use the Reeb graph. This graph was introduced by Reeb [Ree46], based on Morse theory. Given an object surface M and a smooth valued function f defined on it, Morse theory provides the relationship between the critical points of f (points where the tangent plane is horizontal) and the global topology of M. Morse theory states that the shape of the pair (M, f) is represented by the sequence of the homology groups of the level sets (i.e. the set of points x from M such that $f(x)<k$, $k\in\mathbb{R}$. The critical points of f determine the homology groups of M. The homology groups contain the original shape's properties encoded as the number of connected components, holes and cavities of the shape. Its is therefore possible to fully describe the surface of the shape by a finite collection of level-sets, and also get a more complete description rather than simply knowing the global homology. By varying k we can introduce topological changes on the level-sets and obtain a discrete representation of the shape. This can be then encoded into a topological graph called the Reeb graph.

The Reeb graph can be represented as a 1-dimensional skeleton, provided by a continuous scalar function on the surface M. Although the global homology of the surface M does not change as f varies, the topology of the level-sets depends on f. In this way, the choice of f determines a collection of shape descriptors with properties dependent on the function f that characterise the object's surface depending on the application context. Typically, f is chosen as the height function $(\forall p=(x,y,z)\in\mathbb{R}^3,\ f(x,y,z)=z)$ whose critical points (i.e. peaks, pits and passes) are useful for shape description. The main drawback of using the height function is that it produces graphs which are dependent on the orientation of the object in space (not affine invariant). Figures 2.4 and 2.5 show how the Reeb graphs of real and generated data look.

Some research on Reeb graphs, has been carried out using the geodesic distance (which is the minimum length of the paths connecting two vertices u and v of a finite graph) as the mapping function. More specifically, Lazarus and Verroust [LV99], have used the idea of Reeb graphs to con-

struct a skeleton called the Level-Set Diagram, in which the geodesic distance from a source point is used as the function h. Their solution however, is dependent on the choice of source points, and for that reason it is not unique. Different Level-Set Diagrams can be produced for the same model. Hilaga et al. [Hil01], have defined the Multiresolutional Reeb Graph based on the geodesic distance, and used it as a search key for topology matching. The have developed a series of Reeb graphs for an object at various level of details, partitioning the object into regions using the height function at every level.

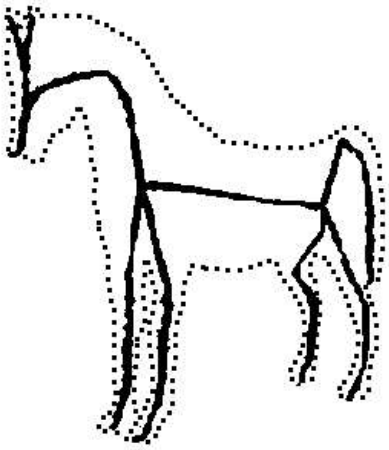

Figure 2.4 Reeb skeleton (bold) of real 3d data (only the boundary of the object is shown here for simplicity)

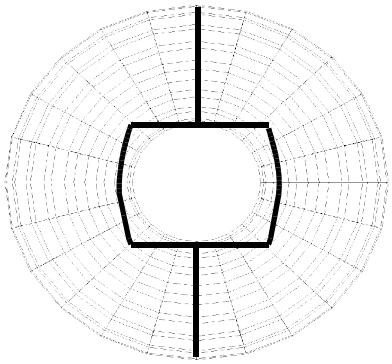

Figure 2.5 Reeb graph of a torus (bold lines). The graph will correspond to the topology of the object.

The skeleton produced by the Reed graph has some interesting properties that make is especially useful as an object recognition and matching key. Firstly, a Reeb graph will always be a 1-dimensional graph structure and will never have any higher-dimensional components such as degenerate surfaces. Secondly, by correct choice of the continuous function *f*, it is possible to obtain a Reeb graph that is invariant to translations, rotations and connectivity changes that occur from simplification, subdivision and re-mesh. The re-meshing property also helps to ensure that such a Reeb graph is quite resistant to noise.

2.1.2 DISTANCE FIELD METHOD

The methods we have seen above might not be suitable for large input datasets. For example, building a 3d Voronoi diagram, given N data points, requires at least $O(N^2)$ computer time complexity [GN00]. Therefore, another equally popular approach is to use the distance field of the object to extract the skeleton. First we construct the distance field of the object, then we find the local maxima of the distance field, and finally we connect these maxima in order to find the skeleton.

There have been several distance field methods proposed for skeleton computation. Most notably, Leymarie and Levine [LL92] have implemented a 2-dimensional MAT by minimising the distance field energy of an active contour model. Zhou and Toga [ZT99] have proposed a voxel-coding method based on recursive voxel propagation. Their algorithm works by using a set of seed voxels and a coding scheme to construct connectivity relationship and distance fields. Bitter et al. [BKS01] proposed a penalized-distance algorithm for skeleton extraction from volumetric data. The algorithm uses a distance field and Dijkstra's algorithm to get a rough approximation of the skeleton, which is then refined by discarding redundant voxels. Wan et al. [Wan01] have proposed a skeletonisation method for virtual navigation based on the distance from boundary (DFB) field, which contains the Euclidean distance from each voxel inside the 3d volumetric environment to the nearest object boundary. Even more recently, Wade and Parent [WP02] have presented a distance field method that uses the Euclidean distance, for automatic generation of the control skeleton of an articulated object (i.e. a skeleton that can be used to control the animation of the object by specifying stick-like skeletons, and often used in this way for animating avatars in virtual environments with the stick like skeletons defined in the H-Anim standard [HAnim]). The discrete medial surface (DMS) is used as a first approximation of the medial axis transform, and via simplification of voxel paths their system produces a relatively good control skeleton for 3d objects.

2.2 THE AFFINE INVARIANT SKELETON

As we have mentioned previously, because the medial axis uses the Euclidean distance, in the form of the radius of bi-tangent circles, it is invariant under Euclidean transformations (rotations, translations and reflexions) but not invariant under special affine transformations (i.e. non-singular linear

transformations composed with translations). Therefore, we can define an affine invariant skeleton as being invariant under the special affine transformation

$$X'=AX+T$$

where X,X' and T are vectors and A is a 2x2 matrix (or 3x3 in the case of 3d skeletons). The transformation is volume and orientation preserving with determinant equal to 1 rather than -1. In practical terms, this means that if a shape is deformed by such an affine transformation, and then its skeleton is computed, that skeleton should be the same as the skeleton computed from the original shape and transformed via the same affine transformation. Figure 2.6 is an illustration of this idea.

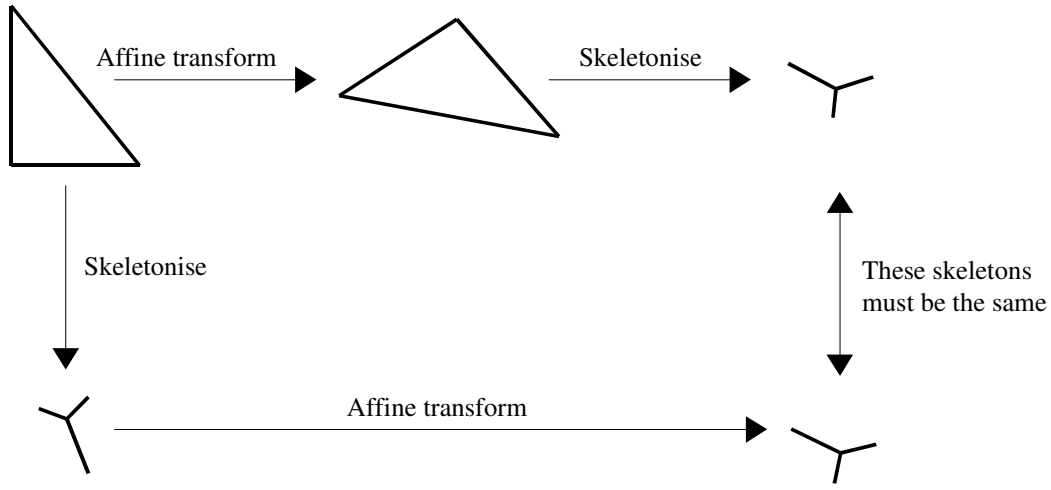

Figure 2.6 Definition of the affine invariant skeleton

2.2.1 IN 2 DIMENSIONS

In [SG98], Giblin and Sapiro defined the affine distance between a point x and a point $C(s)$ on a curve, as the area between the curve and the chord from $C(s)$ that passes through x:

$$d(x,s)=\frac{1}{2}\int_{C(s')}^{C(s)}(C-x)\times dC$$

where $\times$ is the z component of the cross product of two vectors, and *C(s)* and *C(s')* are the points in the curve that define the chord, which contains *x*. This can be seen in Figure 2.7.

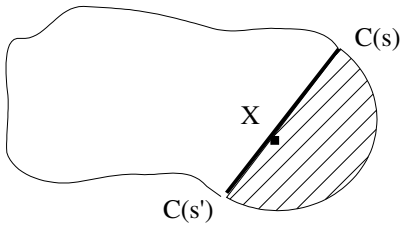

Figure 2.7 Affine distance of a closed curve

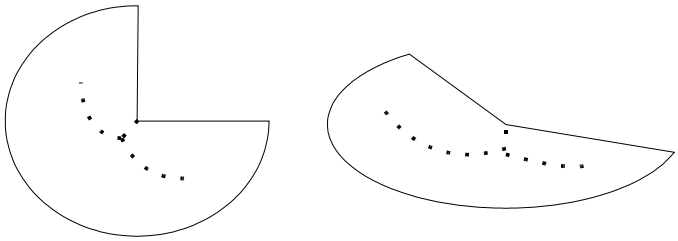

Figure 2.8 Affine skeleton of concave curve and after affine transformation

From here onwards, the definition of the skeleton is similar to that of the medial axis. Thus, a point *x* is said to be on the affine invariant skeleton if and only if there exist two different points *C(s1)* and *C(s2)* which define two different chords that contain *x* and have equal areas *d(x,s1)=d(x,s2),* provided that these distances are defined and they are global minimum. If the distances are just local extrema, point *X* is said to be on the affine area symmetry sets of the curve. This definition of the skeleton is more resistant to noise than the MAT because the computation of the area averages out noise to some extent. Betelu et al. [Bet00] have proposed a numerical implementation of the affine skeleton, the results of which we can see in Figure 2.8. Note that it deforms correctly under affine transformation, unlike the MAT from Figure 2.2 above.

In the same publication, Betelu et al. have defined the affine erosion *E(C,A)* of a convex curve *C* as the set of points x of the interior of C that satisfy

$$E(C,A) := \{x \in \mathbb{R}^2 : f(x) \geq A \geq 0\}$$

where *f(x)* is the minimum distance from a point x to the curve $f(x) = inf\{d(x,s) s \in D\}$, where *D* is the domain of *d(x,s)* for a fixed value of *x*. For a specific *f(x)=A*, we can get the eroded curve *C(A)* which is the boundary of the affine erosion.

$$C(A) := \{x \in \mathbb{R}^2 : f(x) = A\}$$

If we now consider the area *A* to be a time parameter, *f(x)* represents the time the eroded curve takes

to reach the point x. When $A=0$ we have the original curve, and as A increases we get the eroded curve which is inside the original.

There is a close relationship between the affine erosion of a curve and the skeleton, more specifically, a shock point (point of singularity) on the erosion is a skeleton point. This is easy to understand for example for the affine skeleton, if you consider that a shock point x is a point on the eroded curve where two different chords $(C(s_1), C(s'_1))$ and $(C(s_2), C(s'_2))$ of equal area A intersect. x will be equidistant from the curve with $d(x,s_1)=d(x,s_2)$, since the two chords cut equal area, but also the distance will be a global minimum at s_1. This is because x belongs to the eroded curve $C(A)$ and so by the definitions of $C(A)$ and $f(x)$ above, $f(x)=inf\{d(x,s),\ s \in D\} = A$. This ensures that the shock point x is on the affine skeleton.

Recently, Estrozi, Costa and Giblin [LCG03] in order to tackle the affine skeleton for non-convex curves have used polar coordinates to define the curve and re-defined the chordal area as

$$A(\alpha)=\frac{1}{2}\int_{\alpha}^{\alpha+\pi} r^2\, d\theta$$

where α is the angle of the chord and $r=r(\theta)$ is the polar equation of the curve. The skeleton defined this way may produce disconnected axes owing
to inflexions in the curve.

2.2.2 IN 3 DIMENSIONS

There has been an attempt to approximate the 3d affine skeleton by M.S.Jeong and B.Buxton [JB01] in 3d human body scans. Their approach was to calculate the affine skeleton for 2d horizontal cross-sections of the body and then from that create the affine skeleton. Their preliminary results have shown that the produced skeleton is less sensitive to noise than the medial axis, and seems to deformed appropriately under linear transformations.

The 3-dimensional case was proposed by Betelu, Sapiro and Tennebaum in [Bet01], and it is the theory behind the algorithm we are going to use in this project. Extended to 3d, the affine distance becomes affine volume (or chordal volume), and it is the volume enclosed between the object and a chord (cutting plane) at a point *X*, in the direction outwards from the interior of the object. It is known that volumes are invariant under special affine transformation, and because of the averaging effect when they are computed, they are also insensitive to noise. The authors have given three key definitions for the 3d affine erosion, the chord set, the erosion level-set function and the erosion-set.

The *chord set* is defined as follows: Assume a volume (bounded set of points) $V \subset \mathbb{R}^3$, and a plane $\prod$ with normal *n* that contains a point $x \in V$. The chordal set $\sum(x,n,V)$ is the connected set of points inside the volume that contain *x* and that are on the opposite side of the normal *n* of the plane.

The *erosion level-set function E(x,V)* is the greatest lower bound of the volume of all chord sets defined by all points $x \in V$.

$$E(x,V) = \inf_{n \in S} v(\sum(x,n,V))$$

where the *inf* (greatest lower bound) is computed with the normals *n* pointing at all the directions of the unit sphere.

Finally, the *erosion-set* Γ_v is the set of points *x* satisfying $v \leqslant E(x,V)$. In other words, we remove any points *x* from the volume of the object, that have *E(x,V)* below some chosen threshold *v*.

All three definitions are illustrated in Figures 2.10, 2.9, and 2.11 respectively. Note that because the volume of the chord set is only defined for the points that are inside the object and connected to *x*, in Figure 2.10 the small volume (indicated by the arrow) although cut by the plane $\prod$, is not connected to *x* and therefore is ignored.

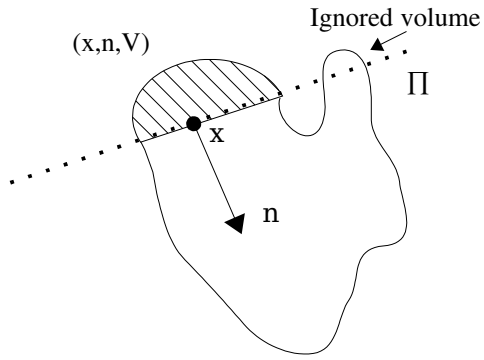

Figure 2.10 The chordal set (shaded) at point x

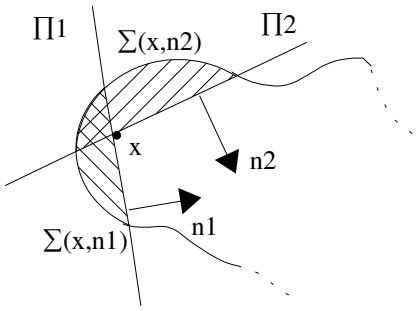

Figure 2.9 The erosion level-set function, will be the smallest chordal set at point x

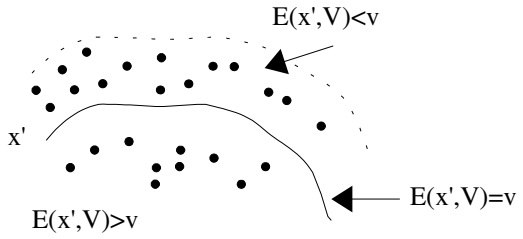

Figure 2.11 The erosion set Γ_v is the set of all the points where the erosion level-set function *E(x,V)* is above a certain threshold.

So, in this case and in an analogous way to the 2d case, the 3d affine invariant skeleton is defined as the shocks (or the discontinuities on the normals of the erosion set) of the contour surfaces *E(x,V)=const* (corners of erosion sets).

According to Betelu et al. [Bet01], the results from the 3d affine erosion seem quite robust even for objects with complex topologies (e.g. with holes). The approximation of the skeleton however, has proven to be a rather more problematic goal to achieve, owing to the inherent difficulty in computing the shock points. Furthermore, because we are now not dealing with Euclidean distances but with volumes, which are slower to compute, the overall computation of the erosion is affected. More specifically, with implementation proposed by Betelu et al. it was estimated that the erosion is $O(N^{5/3})$, where N is the number of voxels in the volume. The bulk of the computation time is spend on computing the erosion level-set function for the volume, and in the next chapter we discuss some ways that we can reduce the running time of the algorithm, and also some ideas on how to deal with the shock computation.

2.3 RECENT SKELETONISATION METHODS

Since the beginning of this project, there have been a few interesting advances in the area of skeletonisation and affine skeletons and it seems that there is particular interest in the study of thin, tree structured 1-dimensional skeletons for use in object recognition or animation, in distinction to the 2d surface like skeletons such as the affine skeleton and the medial axis in 3d.

Perhaps the most significant development in the area of affine invariant skeletons is that of Mortara and Patané [MP02] who they have extended the theory of Reeb graphs to produce 1d affine invariant skeletons. Even though many extensions to the Morse theory have been proposed, the Reeb graph suffers of at least two problems. First it depends on the choice of function f and second there is no distinction between small and large features of the shape, owing to the fact that connected components are collapsed into the same class without any distinction of their sizes. Furthremore, as we have already noted, Mortara and Patané argue that the choice of the height function as the generic function for constructing the Reeb graph, will produce graphs that are dependent on the orientation of the object in space. They propose a definition of the Reeb graph using topological distance from global features, defined by source points in high curvature regions to guarantee that the result is affine invariant, and therefore, not dependent on the orientation of the object in space. Compared with skeletons produced by using the height function, their approach is affine invariant because the chosen function f does not rely on either the coordinate system nor on the surface embeddings. However, if the curvature evaluation process, which is an intrinsic step of their algorithm, does not recognise at least one feature region, their approach is not useful for extracting a description of the shape. On the contrary, the height function always guarantees a result.

Even more recent publications are those from W-C Ma et al. [MWO03] and [Wu03]. In the first, the authors attempt to extract the skeleton from 3d objects by building its distance field by using Radial Basis Functions (RBFs). They then apply a gradient descent algorithm to locate the local extrema in the RBFs which indicate branching or termination nodes of the skeleton. RBFs are continuous functions which is a good property for use in gradient descent, but construction of an appropriate RBF which preserves the geometrical properties of arbitrary 3d models is still under considera-

tion.

In their second publication [Wu03], they use a different approach, based on what they call the Visible Repulsive Force (VRF) to locate local extrema. The author provide three definitions.

The first is the visible set *V(x)*. Assume a point x in the interior of a surface *S*, so

$$V(x)=\{v_i \mid v_i \rightarrow x,\ v_i \in S\}$$ (a→b denotes that a is visible to point b).

Then the VRF is defined as:

$$\overrightarrow{VRF}(x)=\sum f(\|v_i-x\|)\cdot\overrightarrow{(v_i-x)}$$

where $v_i \in V(x)$ and $f(r)=r^{-2}$ is used as as the Newtonian potential function.

Finally, they define the Visual Domain Skeleton (VDS) of the object as

$$D(S)=(Q,M)$$

where *Q* represents the set of local minima in VRF, and *M* an operator used to describe the topological relationship in *Q*. The local minima of VRF are located by first using a radial parametrisation process and then a shrinking procedure. The authors name each of the local minima as VDS nodes, and have determined that each point on the surface *S* will converge to a VDS node. Connecting these nodes based on their neighbourhood relationship on the surface, will produce the skeleton. Although the skeleton produced has both topological and morphological information of the shape, the skeletonisation process is not fully automated, since undesirable connections need to be removed by hand. Furthermore, locating the VRF minima takes 95% of the execution time and for large models it can prove rather a computationally expensive process.

3 SKELETONISATION ALGORITHM

Now that we have covered the theory behind the 3d affine invariant skeleton we will see how it can be implemented in discrete mathematics. This of course presents its own problems since as we will see, even simple arithmetic operations can have many pitfalls when implemented on a floating-point computer system. In this chapter we briefly describe such computational geometry issues and examine the 3d affine erosion algorithm more closely. Problems associated with this algorithm, such as speed and accuracy, and what causes them are identified, and addressed in the section algorithm improvements. Finally, we conclude with a discussion on the issues of computing shock points.

3.1 COMPUTATIONAL GEOMETRY ISSUES

In previous chapters we have seen the theory behind the medial axis construction and other skeletonisation methods, given in the context of continuous geometry. In continuous geometry, an object is defined using a continuous representation, usually as a polygon, polyhedron or some closed curve or surface. Skeletons such as the medial axis and Voronoi graphs are defined using curves, surfaces or continuous approximations of them (e.g. with polygonal meshes).

When the same ideas are applied in computational geometry, there are more approximations involved. An object analytically defined in continuous space, will need to be approximated as a set of discrete points in a rectilinear grid, and in a Cartesian coordinate system. In 2d, the object is said to be pixelised, whereas in 3d it is said to be voxelised.

The skeleton of the object must be approximated as well, and typically, it will be a subset of the points of the discrete object, if we consider the object as a volume and not only as a boundary. The mathematical definition of the skeleton results in a computation of a unique skeleton for any given object. In the discrete case however, there are different approximation methods for constructing the skeleton, and since there is no uniform mathematical definition, there can be noticeable differences between the skeleton of the same object constructed with different algorithms. In addition, whereas the continuous skeleton has the same topological structure as the continuous object, there is no guarantee that the discrete skeleton will preserve the topology of the discrete object. In fact, it is

quite possible that it will be radically different.
Nevertheless, we desire certain properties to be present in the discrete skeleton. These are:

- *Similar topology*: The discrete skeleton should exhibit the same basic connectivity as the original object.
- *Centered*: The skeleton should be as centred as well as possible within the object, with respect to its boundary.
- *Reconstruction*: The set of points generated by the inverse distance transform (if such a transform exists) should be identical to the set of points of the original discretised object.
- *Affine invariance*: When the discrete skeleton is submitted to affine deformation, the resulting skeleton should be the same as the discrete skeleton of the affine transformed discrete object.
- *Noise resistance*: When there is surface noise (presence or absence of individual pixels near the boundary of the object) the discrete skeleton should be similar to the noise-free discrete skeleton.

Working in discrete geometry poses additional difficulties especially when trying to use formulas from continuous geometry. We have faced a variety of problems, because of the floating-point numerical system a computer uses, and the fact that computation results and numerical comparisons are almost never exact. For example, when comparing two vertices that we expect to be equal but which might for instance have been computed as a result of an intersection or a split of a triangle, the comparison will most probably fail. Besides that, every computing platform has its own floating-point system, a fact that complicates things further, if we are looking for portability across platforms. One of the ways to counteract such problems is to introduce a distance threshold, and see if the second vertex falls within a circle (or sphere in 3d) defined by the first vertex and the threshold as its radius (Figure 3.1).

Another equally valid way, is to try and bypass the floating-point system altogether and convert to an integer numerical system. The way to do that, is to multiply all the floating-point values by an integer constant and then round-off the numbers at the closest integer. As long as this is applied con-

sistently throughout, we should be able to avoid most of the problems associated with floating-point numbers in computational geometry.

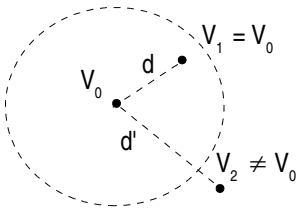

Figure 3.1 Comparing vertices with a threshold. If $d \leq r$ then $V_0=V_1$

Most geometric algorithms are formulated in terms of real numbers, and the problem when trying to implement algorithms in a floating-point system, is the fact that not all real numbers can be represented as floating-point numbers. If we assume that $r \in \mathbb{R}$ and *f(r)* is its floating-point representation, and in order to get from a real number to a floating-point *r* has been truncated or rounded-off to the nearest floating-point, the absolute round-off error will be $|f(r)-r|$.

Arithmetic operators such as addition and multiplication when carried out on floating-point numbers can also introduce numerical errors that will not appear in real number operations. For example, if $r,s \in \mathbb{R}$ and $s \neq 0$, then $r+s \neq r$. However, it is possible that *f(r)+f(s)=f(r)* when *f(r)* is much larger than *f(s)*. Even the properties of addition such as commutativity and associativity can be affected when dealing with floating-point numbers. It is not always true for example that

$$(f(r)+f(s))+f(t)=f(r)+(f(s)+f(t))$$

If *f(r)* is much larger in magnitude than *f(s)* and *f(t)*, it is possible that *f(r)+f(s)=f(r)* and *f(r)+f(t)=f(r)*. Then,

$$(f(r)+f(s))+f(t)=f(r)+f(t)=f(r)$$

which is obviously not equal to $f(r)+(f(s)+f(t))$.

There are many examples like the above, so it is essential not to rely only on mathematical logic when implementing an algorithm. That is why many times the algorithm might appear to be radically different from the actual mathematical theory on which it is based.

3.2 EXISTING ALGORITHM

The algorithm proposed by Betelu et al. based on the theory we have seen in the previous chapter, has two distinct parts. The first is the erosion of the object and the second the computation of the shock points, or more precisely, first the computation of the erosion level-set function for every point x' in the volume, and second the computation of the discontinuities on the normals of the surfaces where $E(x,V)=constant$. We will attempt to describe these two operations distinctly, since it is more efficient to implement and execute them separately from each other. The first operation will erode the object and the second will detect the singularities of the eroded volume.

3.2.1 EROSION

Erosion is a fundamental operation in mathematical morphology, based on Minkowski's subtraction, where the structuring element is a circle (or sphere in the 3d case). However, the affine erosion has a completely different definition, with the majority of the execution involving computation of chordal volumes.

Once we have computed the erosion level-set function $E(x,V)$ for every point inside the volume, the erosion step will be finished, and in principle this could be achieved by computing the volumes of all the chord sets $\sum(x,n,V)$ for every $x \in V$ in all possible directions n on the unit sphere and taking the minimum, just as in the 2d case already defined by Betelu et al. [Bet00] This solution of course, is far from ideal and not very feasible. The number of points in the volume is very large and, when multiplied by the number of possible orientations n we could choose, makes this approach very computationally expensive from a practical point of view. So, Betelu et al. proposed triangulating the surface of the object and using the inwards-pointing normals of the triangles as possible orientations for computing the volumes of $\sum(x,n,V)$. This together with the fact that the volume of a chord $\sum(x,n,V)$ is the same for all the points lying on the same plane can simplify the computation process.

The input to their algorithm is a surface enclosing a connected volume *V*, given implicitly in terms of a level-set function *F(x)*, and discretised in a volumetric array. This kind of surface, is similar to the surface representation of objects used for medical image applications.
The first step is to triangulate the surface using the marching cubes algorithm [LC87]. Once we have a polyhedral representation of the object, we can compute its volume using a boundary integral formula:

$$v_0 \approx \frac{1}{3}\sum_{i=1}^{n} xi \cdot \Delta S_i$$

where n is the number of triangles, ΔS_i is the area of the triangle T_i multiplied by its inwards normal $-n_i$ and x_i is the triangle's centre of mass. The volume calculated in this way is just an approximation to the actual volume of the object obtained by "breaking" the polyhedral representation of the object with tetrahedra with bases the triangles of the object's surface , computing the volumes of these tetrahedra, and summing them. The more triangles there are in the object's surface (i.e. the finer the resolution of the triangulation of the surface), the closest the approximation will be to the actual volume.

Now we can start an iteration, and for every triangle T_i on the surface of the object do the following:

- Define a plane Π that contains the centre of mass x_i of the triangle T_i, with normal that of the inwards normal of the triangle $n_\Pi = - n_i$ (Figure 3.2).

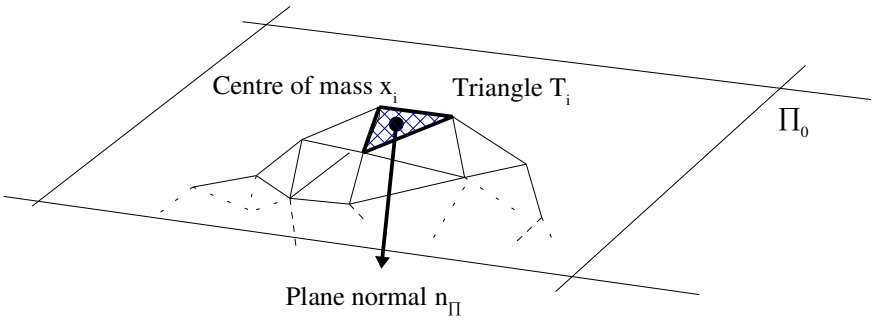

Figure 3.2 Starting point of the algorithm, creating the cutting plane

- Advance this plane along its normal towards the inside of the volume, by a distance

$\Delta d=min(\Delta x,\Delta y, \Delta z)$, where $\Delta x,\Delta y, \Delta z$ is the volumetric grid point spacing. The advanced plane will be:

$$\Pi' \Rightarrow (x - x_i^l)\cdot n_i = 0$$

where $x_i^l = x_i + n_i l \Delta d$ and l is an iteration counter.

While the plane is being moved, we should find the connected chordal points that are inside the volume and under the plane. It is very important to mention that the chordal points must be connected with x_i and inside the object or else the volume they enclose is not defined. What this means is, that there must be a connected path inside the volume to connect x and x' if x' is to be a member of a valid chordal set. Figure 3.3 shows such an example. The valid chordal set is the greyed area, since there is a path to connect every point inside the set with x. Therefore, there is the additional step of determining such connected components.

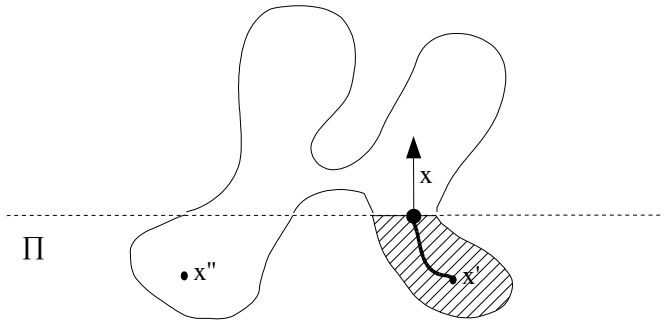

Figure 3.3 Connected components example. x' is connected with x, unlike x'' which is inside the volume but not connected with x.

The boundary of these points will be triangulated (by using marching cubes again) and the volume they enclose computed by means of a boundary integral formula like before, only this time its is for an open polyhedron, where the opening face is planar. So the enclosed volume is given by:

$$v^l \approx \frac{1}{3}\sum_{k=1}^{m} (x_k - x_i^l)\cdot \Delta S_k^b$$

Here ΔS_k^b is the area of the boundary triangles T_k^b each multiplied by their inwards normal and x_k is their centre of mass. The letter b indicates that the triangles are part of the new boundary, and

m is the number triangles in the boundary.

We can stop advancing the plane when $v_i \geq v_0/2$ because according to Theorem 3 from [Bet01], $0 \leq E(x,V) \leq v_0/2$. In other words, it is not possible to find a minimum volume for a chordal set, when the plane exceeds the "middle" of the volume, for that specific orientation (plane's normal). The advancing plane idea is illustrated in Figure 3.4.

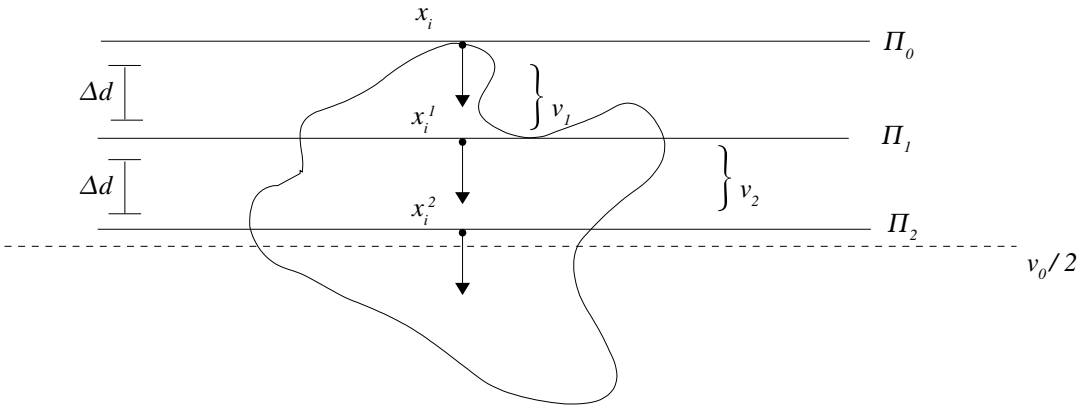

Figure 3.4 We advance the cutting plane and calculate the chordal volumes until we reach $v_0/2$

Now that we have volumes for all the chordal points for every Δd the plane was advanced, we can use linear interpolation to estimate the chordal volume for every chordal point at a distance $l\Delta d$ from the boundary. Of course, the accuracy of the volume interpolation will depend on the value of Δd. The smaller Δd the higher the accuracy. If, however, $\Delta d < min(\Delta x, \Delta y, \Delta z)$, we will not obtain any additional benefits but incur unnecessary computational cost.

Following the above computation of the chordal volumes, we can start calculating the erosion level-set function $E(x,V)$ in an iterative way. For every orientation generated by the normals of the boundary triangles, and every chordal point x we compute:

$$E(x,V) = min(E(x,V), u_{int}((x-x_i)\bullet n_i))$$

where u_{int} is the interpolated volume.

When all the triangles are exhausted, $E(x,V)$ will contain the minimum volume. We also store the the normal (optimal normal) that produces this minimum volume. At the end of the algorithm, we

have a scalar value, the *E(x,V)*, associated with every internal point of the object and also the optimal unit normal *n(x)* associated with it. All these optimal normals generate a vector field that can be used later on to detect shocks.

We are now ready to proceed to the next step, which is the shock detection, but it is quite possible at this point to carry out an affine erosion of the object simply by thresholding. Retaining the points *x* with *E(x,V)* > *threshold* gives us the results shown in Figure 3.5 for a torus:

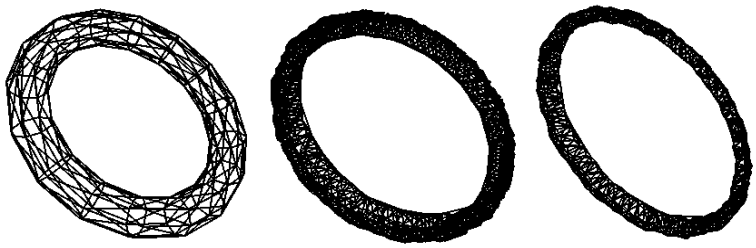

Figure 3.5 Original torus (left) with volume v_0 , affine erosion with a threshold $v_0/10$ (middle) and with a threshold of $v_0/7$ (right).

3.2.2 SHOCKS

So far, we have computed the erosion level-set function *E(x,V)* for every chordal point *x* in the volume and the optimal normal vector *n(x)* that produces this level-set function. To identify which of these chordal points are also skeleton points, we need to detect the singularities on the boundary present as the object is eroded. These will be points where the boundary surface of the eroded object exhibits some kind of singular behaviour, such as a cusp (point where tangent vector reverses sign) or a point of self-intersection. At these points, the partial derivatives of the curve or surface will be singular (in strict mathematical terms, they will be undefined, but the way the surface of the eroded object is generated the derivatives will become very large). This can be seen in Figure 3.6 where skeleton points appear on the corners of the erosion sets.

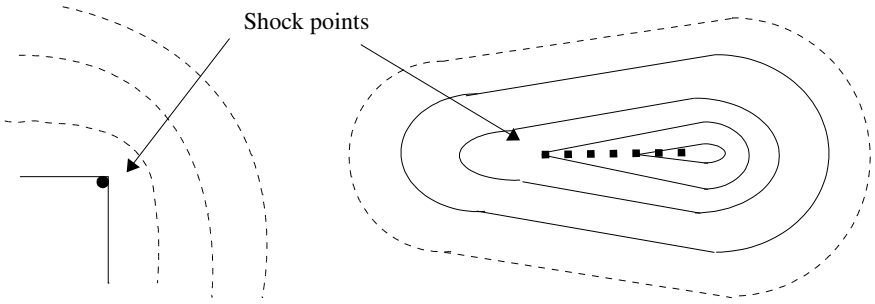

Figure 3.6 Shock points (thick dots) generated from the erosion of the curve

Detecting such points can be accomplished by computing the mean curvature *H(x)* of the surfaces *E(x,V)=constant* as the object erodes, and by keeping those where $|H(x)|>threshold$. The authors [Bet01], propose that the threshold is of the order of the inverse of the discretisation size. That is,

$$threshold = \frac{\alpha}{min(\Delta x, \Delta y, \Delta z)}$$ where α is of the order of unity.

Computing the mean curvature for the surface from the surface of the eroded object is troublesome. Fortunately, the mean curvature is the divergence of the vector field of the optimal normals, and the divergence can be approximated by finite differences. The finite difference is the discrete analogue of the derivative (an infinitesimal change in the function with respect to whatever parameter it may have). The divergence computed by finite differences is:

$$H(x) = \nabla . n(x)$$

where in 3 dimensions, the divergence is, in Cartesian form:

$$\nabla . n(x) = \frac{\partial n_x}{\partial x}, \frac{\partial n_y}{\partial y}, \frac{\partial n_z}{\partial z}$$

Each of the partial derivatives may then be approximated by finite differences in the usual way since *n(x)* is available over a regular grid of vectors. According to the authors [Bet01], the easiest and fastest way to calculate them is to use the intermediate difference operator. With this operator,

for each axis we look at the neighbour and the optimal normal of the current voxel, thus giving us a total of two voxels from which to sample. So, for the x-axis the operator is:

$$\frac{\partial n_x}{\partial x} = \frac{n_x(x+\Delta x) - n_x(x)}{\Delta x}$$

and can be extended in the y and z axes in a similar way. There other operators that can be used that sample from a bigger neighbourhood and thus produce better results, such as the central difference operator $\frac{\partial n_x}{\partial x} = \frac{n_x(x+\Delta x) - n_x(x-\Delta x)}{2\Delta x}$ where we look at the two neighbours at each direction and ignore the value at the current voxel. Therefore we sample from six neighbouring voxels. Other operators, such as the 3d Sobel, Prewitt and Zucker and Hummel, sample from even larger neighbourhoods, producing better results but have a slightly higher execution speed[3]. We will examine such operators later on this chapter.

In conclusion, these are the two steps necessary for computing the skeleton. However, there are two important drawbacks of this algorithm that can affect the computation of the 3d affine skeleton. The first is associated with the erosion and its computational complexity. According to the authors [Bet01], the algorithm is of $O(N^{5/3})$ with computation time being distributed as: triangulation of the boundary of the chord sets by means of the marching cubes algorithm 33%, connected components 53%, and computation of chordal volumes 14%.

The second problem is associated with the calculation of the shocks and concerns accurate computation of the divergence. It is quite difficult to accurately isolate shock points by using a discrete approximation of the mean curvature. This is because sometimes discretisation effects can lead to very high value of the derivative estimates with the result that points can be mistakenly chosen as points of high curvature and thus as skeleton points. In the next sections we look at some alternative ways of alleviating some of these problems, and improving the algorithm.

3 For example the central difference operator is four times faster than the Zucker-Hummel or Sobel 3D.

3.3 OUR IMPROVED ALGORITHM

From here onwards, we will examine some ideas on how to improve the efficiency and effectiveness of the skeletonisation algorithm.

We start with a change to the input to the algorithm, which is going to be a triangulated surface in an OFF file format [Geom]. The OFF format contains the vertex data followed by the faces (connectivity) information. This pre-calculation of the triangles, enables us to avoid having to use the marching cubes algorithm. Avoiding such calculations at the beginning of the algorithm and also every time we advance the plane, will save us an estimated 33% of the computation time
When it comes to using human body scans produced by the Body Line scanner, it is necessary to do some preprocessing before we could convert them to the OFF format. The scanner software will produce a cloud of 3d points that approximate the surface of the body. According to [OJ03], any noisy vertices will be removed through filtering by using a model cleaning software provided by Laura Dekker. This software will produce inventor files [SGIInv] with either a hierarchical or single mesh, with the possibility of there being holes and non-manifold portions. Joao Oliveira produced software to read these inventor files, delete any non-manifold parts of the mesh, and to fill the holes using a simple centroid algorithm. In addition, Joao's software performs some minor repair work such as pushing out dents in the arms and so on, before saving the mesh in an OFF file.

Using a pre-triangulated file however, means that we have to generate points inside the volume that will be used later as chordal points. The best way to do this is by creating a bounding box around the object, create points at specific intervals in the box and determine which of these points are also inside the object. There are different choices for bounding boxes, the easiest one to implement being the axis-aligned box, which has dimensions the minimum and maximum vertices of the object in every dimension. This may however enclose an unnecessary large volume so if efficiency and computation speed are important, it should be avoided. The next choice is an object-axis-aligned box, where the principal axes of the object are used to fit a box that encloses the volume. The best choice will be a minimum bounding box obtained by computing the diameter of the point set, such that described by Barequet and Har-Peled [BP01]. This will enclose the smallest volume and so will produce the fewest points outside of the object. For our implementation we used the axis aligned

bounding box, since it was easiest to program and to generate points at specific intervals without having to define its dimensions in parametric form.

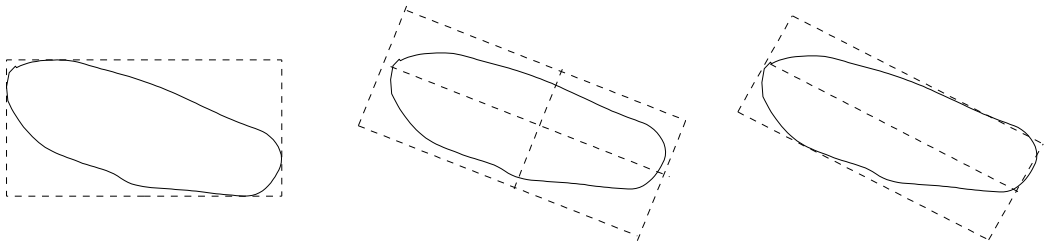

Figure 3.7 The three different types of bounding boxes. From left to right: axis alligned, PCA and minimum volume

Once the bounding box has been created, we begin generating points inside the box at discrete intervals $\Delta x=\Delta y=\Delta z$. The next step is to determining which of these are also inside the object (polyhedron). We do this by casting random rays from the point of interest and determine how many times it will intersect the boundary (i.e. how many triangles it will intersect). If we have an odd number of valid intersections then the point is guaranteed to be inside the polyhedron, whereas an even number will indicate that the point is outside and could therefore be safely discarded. By valid intersection, we mean that the ray intersects a triangle inside and not at an edge or vertex. A vertex or edge intersection cannot accurately indicate if the ray passes through or just touches the boundary, and as a result it is not possible to determine if the point is inside or not. If such an intersection exists, we cast another random ray.

Determining if we have a valid intersection is quite straightforward and it is an approach based on the work of Möller and Trumbore [MTT97]. If we define a triangle as a sequence of vertices (V_0, V_1, V_2) a point P inside the triangle can be defined in terms of its position relative to theses vertices. So: $P=wV_0+uV_1+vV_2$ where w,u,v are the barycentric coordinates of P and $w+u+v=1$. Because $w=1-(u+v)$, frequently just the pair u,v is used. Thus we can determine whether an intersection point is within a triangle or somewhere else on the plane in which the triangle is lying by inspecting the values of u and v. If $0 \leq u \leq 1$, $0 \leq v \leq 1$ and $u+v \leq 1$ then the intersection is within the triangle. Otherwise, it is in the plane but outside the triangle.

The next part of the algorithm is similar to Betelu's solution, where we select a triangle, define a plane from the centre of gravity of that triangle and the normal towards the interior of the volume, and start advancing the plane in a similar fashion. The major difference between our algorithm and Betelu's algorithm is that every time the plane is advanced we do not need to use marching cubes to calculate the boundary of the chord set, since we already have triangles. All we need to do is find which triangles intersect the advancing plane, cut and reconstruct these triangles while keeping the rest of the object's surface as it was. The boundary triangles below the plane together with the reconstructed triangles below the plane, will form the new boundary of the chordal volume and then we can go on to calculate the volume in the same fashion as before. The cut and reconstruct idea is illustrated in Figure 3.8.

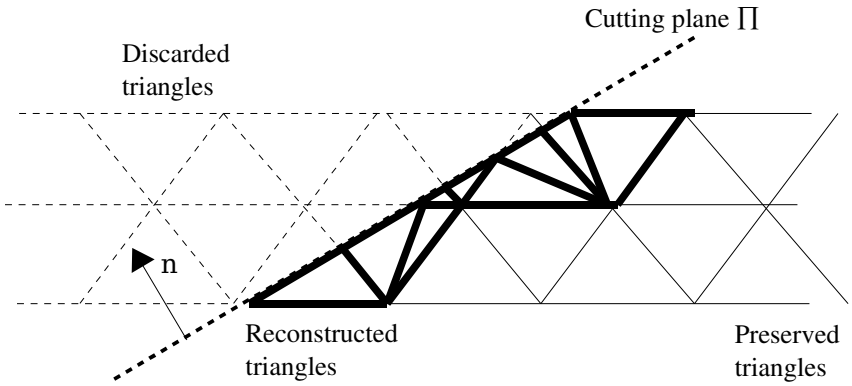

Figure 3.8 Cut and reconstruct process. Reconstructed triangles (bold) together with the triangles under the plane form the new object's surface.

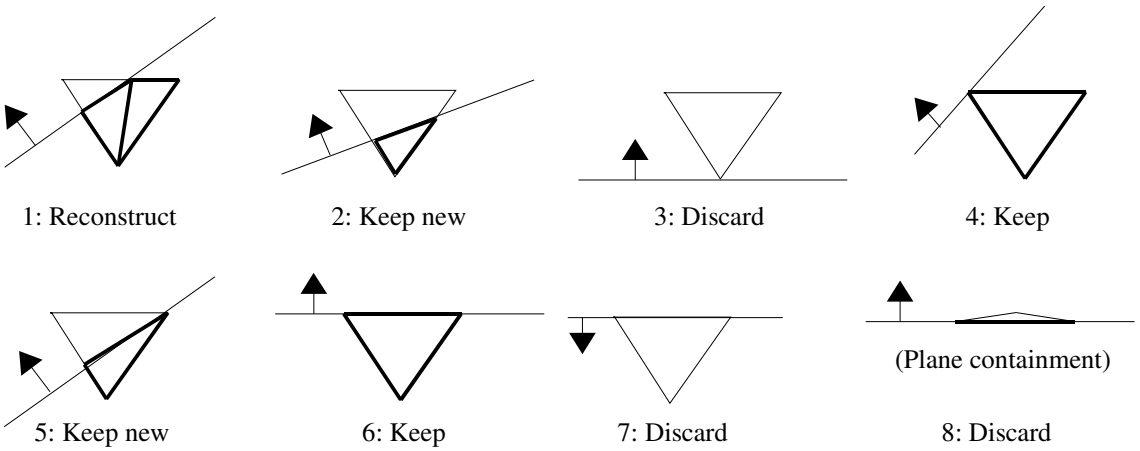

Figure 3.9 The eight possible ways a triangle can intersect with a plane and how it can be reconstructed

This cut and reconstruct strategy, makes using the marching cubes algorithm obsolete, provided of course we have a pre-triangulated surface. If we start with a point cloud, such as typical medical imaging data, we can use marching cubes or some other triangulation algorithm (e.g. [PWH98]) at the beginning and still use this cut and reconstruct solution to avoid triangulating the surface every time the surface is advanced. Cutting and reconstructing triangles is very simple. We just find the intersections between the plane and every triangle, and then depending on the way the plane cuts the triangle as we can shown in Figure 3.9, we reconstruct accordingly.

For complex shapes, for example non-convex objects, the plane might cut the object into more than one connected component so it is necessary to determine how many components exist after we cut and reconstruct the triangles. To do this, we use a simple formula. Initially, all triangles are marked as unvisited. Starting with an unvisited triangle, the triangle is marked as visited. For each unvisited triangle adjacent to the initial triangle (the maximum can be three), a traversal is made to that triangle and the process is applied recursively. When all adjacent triangles of the initial triangle have been traversed, a check is made on all triangles to see if they have been visited. If so, the mesh is said to be connected. If not, the mesh has multiple connected sub-meshes, each called a connected component. Each of the remaining components can be found by starting a new recursive traversal with any unvisited face. We finish our search for connected components when all triangles are marked as visited.

It is now necessary to see which chordal points are inside which connected component, so a simple containment check can be used here, similar to that used above, at the beginning of our approach, to determine the bounding box. However, it is possible that the point x_i, which defines the advancing plane, might be outside the object or any connected components. This means there is no chord defined and therefore no volume. So, if we can check whether this is true or not, we can avoid computing unnecessary containment of chordal points. We could test x_i for containment in exactly the same way as above, but we have to pay special attention because in this case the boundary of the chord is going to be an open polyhedron. Therefore a slightly different approach is necessary, which involves including the plane as a possible lid to the open polyhedron. Before that, an attempt was made to reconstruct and triangulate the lid of the open polyhedron[4]. This was successful, regardless of the increased difficulty[5], but the additional computation cost did not counteract any benefits of this approach. We therefore modified the containment check to deal with open polyhedrons, and used the boundary integral formula from section 3.2 above, to approximate the volume of the open polyhedron without any problems. Also, if the random ray will intersect any triangle edge or vertex as we seen before, we just cast another random ray, instead of trying to determine if the ray crosses the boundary or just touches it.

The rest of the algorithm is quite similar to that of Betelu et al. [Bet01], and we stop advancing the plane when $v_l \geq v_0/2$ which is the half of the total volume of the object. Another interesting point to mention, is that Betelu's solution does not include any other criteria for when the cutting plane should stop. So in theory, the $v_0/2$ criterion might never be met, especially for non-convex objects where the plane can exit the object but still $v_l < v_0/2$. It is therefore, quite possible that the algorithm implemented in such a way will keep on iterating forever. See Figure 3.10 for a case when v_l will always remain less than $v_0/2$.

There are many solutions to this problem, the simplest of which is to check that $l\Delta d$ does not exceed

4 Note that after cutting and reconstructing the triangles the polyhedron will remain open where the cutting plane was.

5 In 3-dimensional computational geometry intersections between points and rays do not really exist. Such intersections are approximated with minimum distances. Trying to triangulate a polygon in such circumstances, is a very complicated and time consuming process, where the problems of computational geometry described previously in section 3.1 are fully realised.

the main diagonal of our bounding box, and when it does, we can stop advancing the plane. We call this method the diagonal distance. The other way, is to cast a ray from the current point x_i and intersect it with the sides of the bounding box, making sure that the distance of the line segment between x_i and the intersection point has not been exceeded by $l\Delta d$. Another way, which is the one we have implemented, is when x_i exits the volume, to cast a ray in the same direction as the normal of x_i, and see if there are any re-entry points to the volume. If re-entry points are found, we can advance the plane Π directly to the first re-entry point. This of course will require us to check for intersections between the ray and every triangle in the boundary of the object, every time x_i exits the volume. If the object contains many triangles, this might not be the best choice, since intersection checking can take a long time. An even more efficient way would be to determine the entry and exit points of x_i at the beginning, before we start advancing the plane, so we know that when the number of entries have been exhausted, x_i will never be back in the volume, and thus we could safely stop the iteration with that specific triangle and carry on to the next. An illustration of the diagonal distance and ray-casting solutions are provided in Figure 3.11.

This is a very important issue, because it can considerably improve the running time of the algorithm and even if the $v_l \geq v_0/2$ criterion is met, we can still see substantial improvements, where the plane can be advanced straight to the next entry point. Table 3.1 shows just how this solution can affect the running time of the algorithm. Note that the improvement increases are not uniform from one object to the other, but rather that they depend on the topology of the object (voids inside the object, how many times x_i^l exits and re-enters and so on). So using the ray-casting method instead of the diagonal distance on a sphere is not expected to bring about any noticeable improvement.

	Execution time	
Method	Body *(292 triangles, Δd=200 pixels)*	Torus *(256 triangles, Δd=200 pixels)*
Previous algorithm	Infinite loop	Infinite loop
Diagonal distance	6h 37m 2 sec	3 h 18 m 37 sec
Ray-casting	47 m	5 m 34 sec

Table 3.1 Different methods for stopping the advancing plane and their impact on execution time[6].

6 The program was executed on a dual Celeron 550 Mhz PC with 194MBytes of RAM.

So, after all our emendations the final algorithm is as follows:

1. *Read the triangulated data*
2. *Compute the volume v_0 of the object*
3. *Generate points inside the volume*
4. *For each triangle T_i in the object do*
   - *4.1.Compute its normal n_i and centre of mass x_i and set iteration variable l*
   - *4.2.Define a plane Π with normal n_i containing x_i*
   - *4.3.While $v<v_0/2$ do*
     - *4.3.1.Increment l*
     - *4.3.2.If $l\Delta d >$ bounding box diagonal break*
     - *4.3.3.Advance plane Π by Δd*
     - *4.3.4.Cut and reconstruct triangles under the plane*
     - *4.3.5.Find connected components*
     - *4.3.6.Find in which connected component x_i^l is contained*
       - *4.3.6.1.Compute the volume of this connected component*
       - *4.3.6.2.Find all the chordal points x' inside the connected component*
       - *4.3.6.3.Interpolate to find the volume of the chord when the plane is at x'*
       - *4.3.6.4.Set $E(x,V)=min(E(x,V), u_{int}((x-x_i)\cdot n_i))$*
       - *4.3.6.5.Store optimal normal n for x'*
   - *4.4.End while loop*
5. *end for loop*
6. *For every chordal point x'*
   - *6.1.Find the divergence of the optimal normal N field*
   - *6.2.If divergence > threshold output to skeleton file*
7. *End*

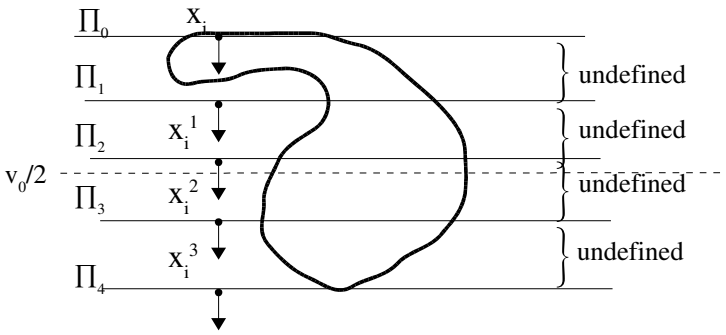

Figure 3.10 The problem of the forever-advancing plane. This is when x_i is outside and the chordal volumes are undefined

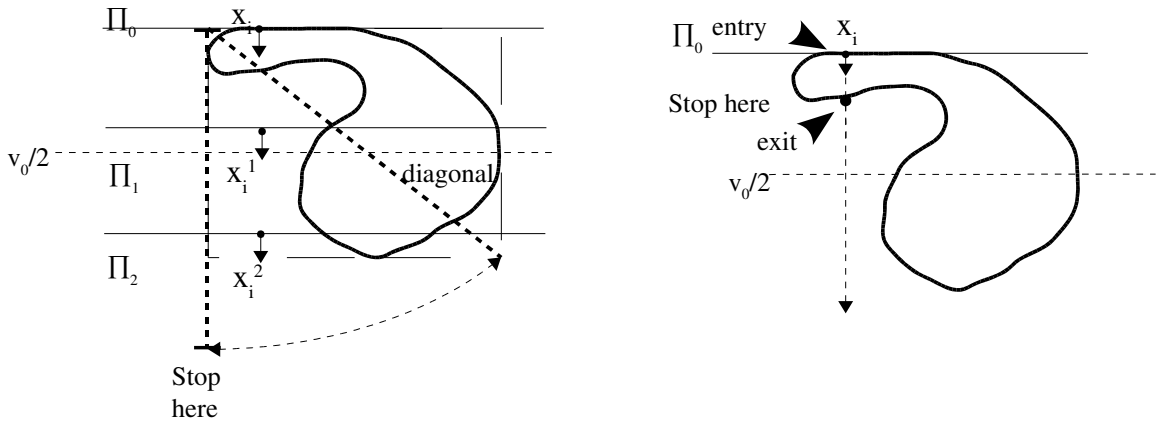

Figure 3.11 Some solutions to the forever advancing plane problem. Using the diagonal distance (left) and ray-casting to detect entry and exit points (right). It is obvious that from the example sketched, the ray-casting method is in principle far superior to the diagonal distance.

3.4 SHOCK COMPUTATION

Let us consider a shape represented by a curve $C_0(s)$ undergoing a deformation, where s is the parameter along the curve and let each point of this curve move by some arbitrary amount in some arbitrary direction, according to Kimia et al. [KTZ95] the evolution of the curve can be described as:

$$\left\{\begin{array}{rcl} \dfrac{\partial C}{\partial t} & = & \beta(s,t)\vec{n} \\ C(s,0) & = & C_0(s) \end{array}\right\}$$

where $\vec{n}$ is the outward normal, t is the time duration (magnitude) of the deformation and β is arbitrary. Furthermore, the deformation could be a linear function of curvature $\beta=\beta_0+\beta_1\kappa$. In this case, the space of all possible deformations is spanned by two parameters: the ratio of the coefficients β_0/β_1 and time t, which constitute the two axes of the reaction-diffusion space. In this space, a shape can be described by a set of shocks that develop during the evolution. These are points where some information is lost during the deformation process, such as discontinuities of the normals of the shape's boundary or the collision of remote portions of the shape through its interior. The connection between shocks and the skeleton is that the reaction axis corresponds to a grassfire simulation,

and the set of shocks that form along that axis, give us Blum's skeleton. There are also shocks that form along other axes of the reaction-diffusion space and according to Kimia et al., they can be classified into four types:

1. A first-order shock is a point of discontinuity in orientation of the boundary of the shape. Intuitively the shock is formed by a protrusion or corner point in the boundary.
2. A second-order shock is a point where two distinct non-neighbouring boundary points joint, but none of their immediate neighbours collapse together. Intuitively, it is formed just before a splitting of the shape into two parts at a "neck".
3. A third-order shock is a point where two distinct non-neighbouring boundary points join such that the neighbouring points also collapse together. Intuitively, a collection of third-order shocks can be thought of as a bend.
4. A fourth-order shock is formed when a closed boundary collapses into a single point. Intuitively, in terms of the evolution a fourth-order shock is a "seed" from which a shape is born.

Figure 3.12 shows typical examples of all types of shocks.

Although intuitively, the above definitions of shocks cannot be easily used in algorithms for shock detection, it is possible to use standard techniques such as central differences or gradient operators. However, these methods will only detect first-order shocks. As we have seen above, the original algorithm used finite differences for shock detection. We used a slightly better method, the Zucker-Hummel operator [ZH81] to detect the gradient and therefore compute the derivatives in the x,y,z directions.

The Zucker-Hummel operator samples all 27 neighbours in a 3x3x3 grid and smooths out the gradients much better than the central differences operator. Furthermore, preliminary tests with our data have shown it to better approximate the divergence and the behaviour of the thresholding used to detect skeleton points seem to be more stable than previously, in a variety of data. Results from this gradient operator are presented in chapter 6, and the definition of the operator can be seen in the ap-

pendixes. The Zucker-Hummel operator produces results equivalent to those obtained with a 3d Sobel gradient detector, the masks for which can also be found in the appendices.

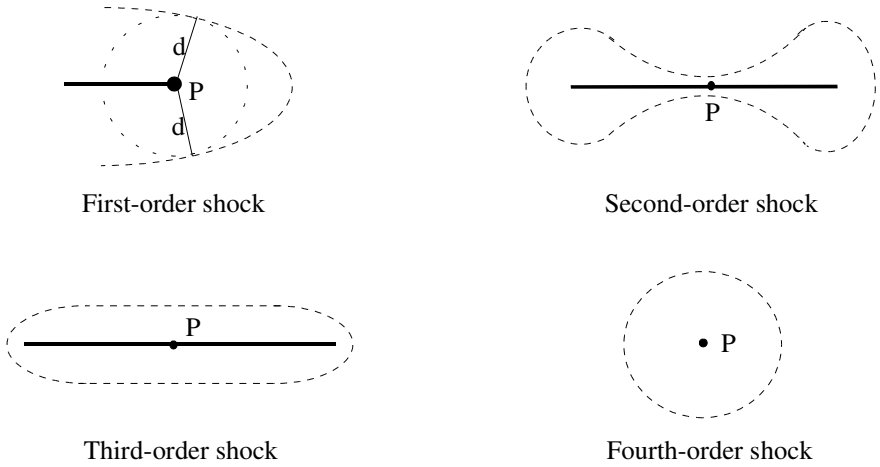

Figure 3.12 The four types of shocks created during the deformation process

However, such standard techniques blur across discontinuities, which is where shocks usually lie, and provide unreliable estimates of geometric quantities, such as orientation. Such quantities are important for shock detection and estimating of shock velocity, which for example may be used to group shocks. In addition, detection of higher level shocks cannot be carried out by means of such methods, and also detection of shocks on a discrete grid is a difficult problem. Shocks occur as discrete events in time and space. It is very easy to miss them if computations are restricted to grid points, and not taking advantage of the continuous propagation information that exists in curve evolution. Finally, distinguishing between singularities that are discretisation artefacts and those that are weak but structurally valid shock points is also a problem. This is similar to the edge detection dilemma, where we are looking for a distinction between weak edges and false positives. The solution used there, for example with the Canny edge detector [Ca86], was to carry out the detection task in two stages. A local detection stage, identifying true as well as some false edges, and a global interpretation stage, which strengthens edges through a relaxation process.

Siddiqi and Kimia [SK96], have proposed a similar method for shock detection, by not only relying on better (sub-pixel) shock detection and classification, but also on the creation of a shock grammar

to detect global interactions between them. This shock grammar enables us to rule out impossible combinations and to group shocks into connected components. This can lead to a hierarchical representation, functionally related to the object's parts, protrusions and bends.

Even more recently, Siddiqi et al. [Sid99] have introduced a new algorithm for divergence based skeletonisation by simulating the eikonal-equation. Their method is based on Hamiltonian physics that offers a number of computational and conceptual advantages for shock tracking. Although the resulting skeleton is not affine invariant, they proposed a more efficient and robust algorithm for divergence computation and shock detection. Their idea is based on the fact that when shocks are formed, the conservation of energy principle in the Hamiltonian system will be violated and energy will be absorbed. This loss of energy can be used to detect shocks. By using the divergence theorem, it is possible to detect the net outward flux per unit volume (when considering a volume with an enclosed surface). Where the flux is negative, indicated areas where energy is lost (sink points). These sink points are also the shock points. However, there is considerable work to be done in this area especially in the simulation of the eikonal-equation in 3d and also on the proposed algorithm for divergence calculation. We have tried to use their idea instead of using a gradient operator, but the results where not that satisfactory, as we will examine in later chapters.

4 ANALYSIS AND DESIGN

This chapter describes the introductory phases of our software engineering process, in which the requirements for the software are established and specified in detail for further development. We start with a data-flow model, to illustrate how data is processed by the system. We continue with the requirements definition, which is an abstract description of the services the software should provide and the constraints under which it must operate. We conclude with the design of the software, followed by a brief discussion of why the particular design was chosen over competing methodologies, and any problems we had to overcome.

4.1 REQUIREMENTS AND SPECIFICATION

4.1.1 DATA-FLOW MODELS

What follows is a series of data-flow models, produced as part of the analysis process which help depict the relationships between the system components and the system and its environment. Furthermore, they depict how data flows through a sequence of processing steps, and how it is transformed at each step before moving to the next stage. We start with the context diagram, where the overall skeletonisation system is illustrated together with the data that moves in and out of its boundaries, to the environment (the user). The triangulated object and the skeletonisation parameters are passed as input, they are processed by the system and the output is the skeleton, with the option of the eroded object as well.

If we pay closer attention to the skeletonisation system (level 1) we can see that it is composed of two main processes, the affine erosion and the shock detection. The skeletonisation process will calculate the erosion level-set function (E.L.S.F.) for every chordal point x' and the optimal normals that produce this E.L.S.F. These data are passed to the next process, which together with parameters input by the user, are used to detect the shocks and thus the skeleton points. Going down to a final level of detail (level 2), we can see the sub-processes for affine erosion and shock computation. These are self-explanatory, since they follow the logic of the algorithm given in section 3.3.

Context diagram

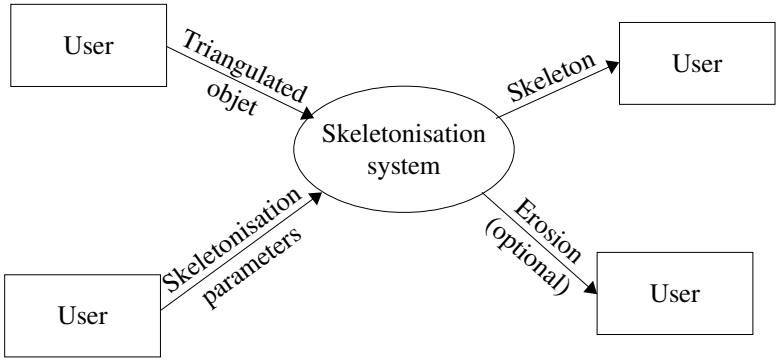

Level 2: Affine erosion

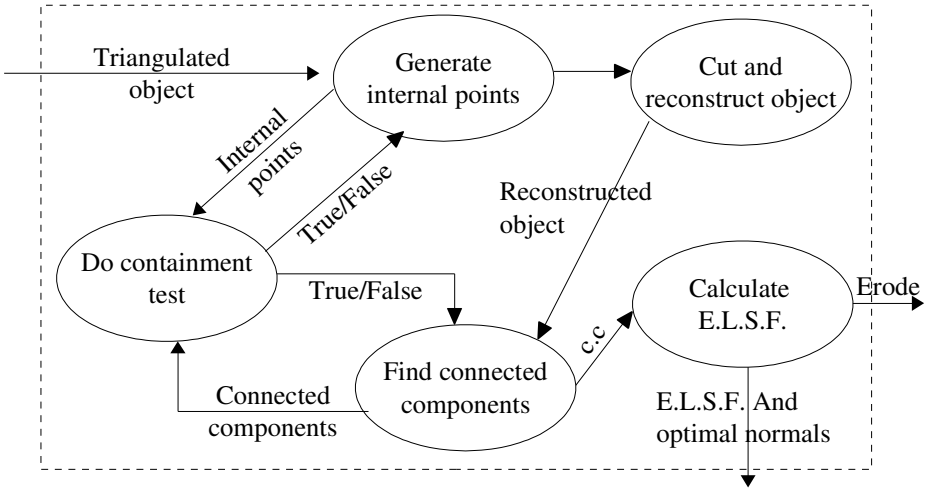

Level 1: Skeletonisation system

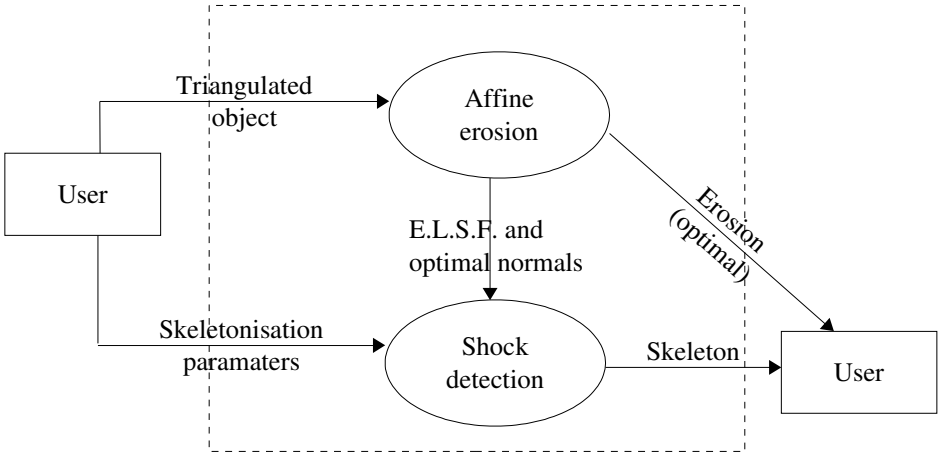

Level 2: Shock detection

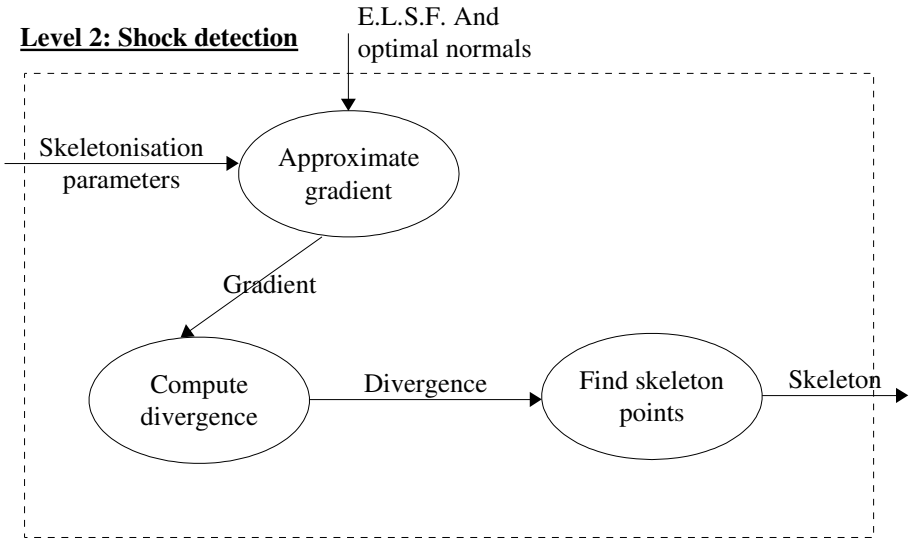

4.1.2 REQUIREMENTS DEFINITION AND SPECIFICATION

Having a basic system model with which to work, we will now examine the requirements of this system. This is basically a more precise description of the functionality of the system, and under what constraints it should operate. We will start with the definition of the requirements, which only depicts the external behaviour of the system and are not concerned with any design characteristics. We have divided requirements into functional, which are just statements of the system services, and how the system should react to particular inputs, and to non-functional, which are constraints imposed on the functionality of the system and the development process.

Functional requirements

Read input data from user

The system should have the ability to read and process input parameters from the user and also read a triangulated polyhedron from an OFF file. It should store the OFF file in computer memory in such a way that it can be processed later by other parts of the system.

(1) The user inputs erosion and skeletonisation parameters together with the triangulated object when running the program.

(2) The system stores the parameters in appropriate variables for later processing.

(3) The OFF file is opened, the data is read and stored so that processing (such as fast sequential access, copying and so on) is facilitated.

Erosion

The system should use the stored object data and by following the steps that the algorithm stipulates, it must calculate the E.L.S.F.s for every point inside the object and if the user requires it to erode the shape, it must do so.

(1) Access the stored triangulated object data, and carry out what is describe in the algorithm, in computational geometry, without affecting the original data.

(2) Provide functionality, including to other parts of the system, such as: point containment testing, volume approximation, connected components detection, shape reconstruction

and E.L.S.F. computation for every chordal point.

(3)Store the output of the processing (E.L.S.F. and optimal normals) to a file, or in memory so that it can be accessed by the skeletonisation sub-system.

(4)If necessary, erode the shape and output the eroded data to a file in an appropriate format (e.g. 3d vertex data), so that is could be displayed by conventional 3d data viewers such as [GLD03].

Detect shocks

The system should read the eroded data (E.L.S.F. and optimal normals) and by using an appropriate gradient operator or other method detect which points are shock points. This shock points should then be written to a file.

(1)Read the optimal normals and use a 3d gradient operator to approximate the divergence.

(2)Detect the shock points by using a simple threshold.

(3)Write these shock points to a file, in a conventional format.

Non-functional requirements

Usability: Based on projects of similar size and functionality we have concluded that since the system requires no user interaction and supervision, apart from the initial data and parameter input, users should be able to use all the system functions with minimal training.

*Portability:*The system should be implemented in a language where it would be possible to compile it for different platforms. The obvious choice would be STD C++, and if possible ISO C++.

Reliability: Based on current systems and user requirements, the system must have a mean time to failure of 4 weeks of continuous execution, considering that most 3d objects with medium to high level of detail, will take >1 week to compute.

Delivery: The software must be completed on schedule and all the necessary testing and documentation must be carried out. On schedule here means by the submission deadline of the CVIPGS MRes

project dissertations.

Robustness: There must be zero probability that the of the original data might be corrupted, and low probability of corruption of the produced data, after failure.

Speed: The design and implementation of the system (together with choice of language) should not considerably increase the estimated execution time of the algorithm.

4.2 SOFTWARE DESIGN

At the beginning of the design process, we chose a procedural design for our software, similar to the one suggested by Betelu [Bet01]. However, it was obvious in that stage, that many parts of the system required input and functionality from other parts, and this proved to be quite complicated for a procedural design to handle. Furthermore, as the scale of the design increased, and many portions of the system were constantly reused, we soon realised that perhaps it would have been better to use an object-oriented (OO) methodology to capture this complexity, the communication needs and code reuse requirements. In addition to that, this project is largely based on computational geometry, which itself is built from simple components such as points, lines, angles, and so on, which are combined in order to build a more complex structure. OO design can capture this behaviour easily because of its special characteristics, such as inheritance, aggregation, data abstraction and so on.

4.2.1 OBJECT ORIENTED DESIGN

So, what follows is a a class diagram (Figure 4.1), which contains the set of classes, and their relationships. This diagram aims to capture the static design view of the system. What is interesting to note from this diagram, is that akin to the bottom-up way that computational geometry is built, so is our system. We can see the *Vertex3D* class as being the building block of our system, and from that, almost all other classes emanate. Another thing to note, is the *Polyhedron* class, which has most of

the functionality of our system, and therefore the most attributes, methods and importance. A polyhedral object and the operation on it, was the main focus of our algorithm, and therefore most of the implementation time and effort was based around the methods of this class.

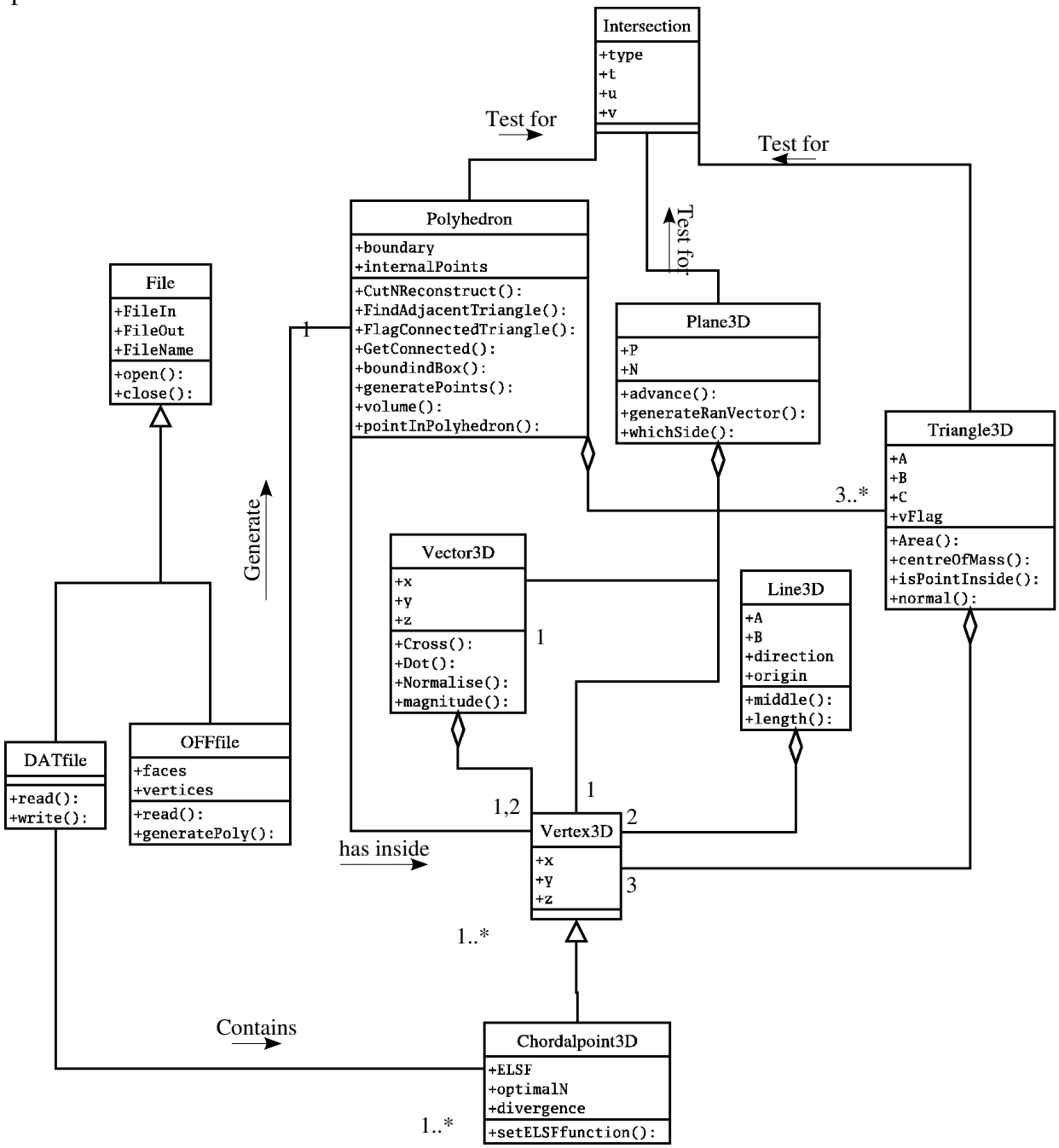

Figure 4.1 Class diagram of the skeletonisation system

The next figure (4.2), is an object collaboration diagram, which shows the organisation of the objects that participate in an interaction, in an attempt to capture the dynamic view of the system. We have only modelled the calculation of the E.L.S.F. since that is the most important and complex operation. We can see the messages between the objects been passed in the appropriate sequence, to generate one iteration of our algorithm (i.e. one advancement of the cutting plane). As we can see here, the polyhedron object is the main object in computing the erosion, and most of the processing is done by function calls instantiated by the object itself. As we can see from the two diagrams, most of the other objects are not directly associated with the actual execution of the algorithm, but through the attributes and methods of the polyhedron and cutting plane.

It would be equally valid, instead of using a bottom-up approach and starting from the vertices and triangles, to use a top-down methodology and create only a few high-level classes (such as the polyhedron) and include the vertices, triangles and so on, as attributes. Although this idea would work, it would resemble a procedural design, and so defeat the point of using an object-oriented methodology in the first place. Scaling a system of that procedural type would be quite difficult, especially if we discover during the implementation that using a polyhedron is not practical. Using a building-block idea like that describe above, enables us to add and remove classes from our system as necessary and to make alterations without affecting other classes. Furthermore, it is easier to port the system, as a collection of libraries, to another platform, to insert new libraries (such as polygons, tetrahedra etc) that follow this bottom-up approach or even to be used as new building components in another system that uses computational geometry.

5

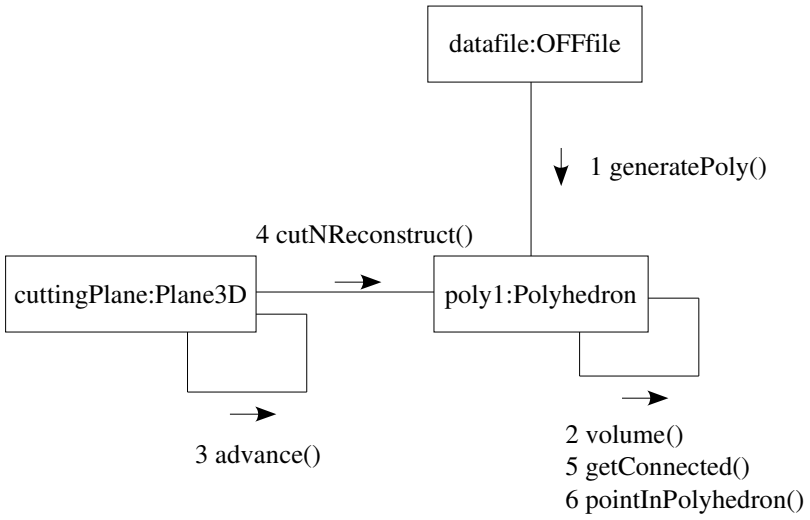

Figure 4.2 Object collaboration diagram for compute ELSF functionality

IMPLEMENTATION AND TESTING

This chapter presents some of the most important issues and difficulties we had to face during the implementation process, and what steps we took to overcome them. We go on to discuss the details of the algorithm complexity and attempt to approximate it using a qualitative approach. We conclude with the testing results, which aim to expose errors in the implementation and determine the capabilities of the system.

5.1 IMPLEMENTATION ISSUES

Our implementation follows the initial design quite closely, with only a few minor modifications made, such as a few additional attributes in some classes, like boolean flags and so on. We originally implemented a linked-list template that we could use with different types of variables and store different data, such as vertices, boundary data and so on. Because most of message and parameter passing between objects is done via pointers, our linked-list template proved to be very unstable under such circumstances and caused random segmentation faults. Furthermore, because of the fact that it allocated memory for variable storage, but did not de-allocate it appropriately, it generated severe memory leaks. If we consider that the program executes over a long period of time, this would cause serious problems and even cause the operating system to halt.

We therefore decided to overhaul the whole system and use the C++ standard template library (STL) and most specifically the vector class. This is a linked-list template similar to ours but without the serious memory leak problems. There are still a few minor memory leak, but there are so small that they do not pose any immediate threat to the execution of the program, even if it is has been running for a considerable amount of time (Table 5.1). In the first three rows we can see the average number of bytes allocated in every main iteration (approx. 1.8Mb) which are stabilised from iteration to iteration, and the growth is insignificant. This growth, can be seen in the identified memory leak, which is 4Kbytes x 2 of non-reoccurring memory loss. This happens once the bounding box is created, and a 24byte x 2 reoccurring once in every major iteration. For a modern workstation with hundreds of Mbytes of memory, a 48byte leak is really not a problem. We could easily fix this problem, but considering Pareto's law its probably not worth the actual effort.

For some parts of our implementation, we had to use the theory and algorithms from [SE03] that we adjusted and added to our existing system. Particularly, we used libraries for intersections, connected components detection and some definitions of primitives in computational geometry. The fact that we had designed our system using OO methodology, proved a good strategy when using other open source libraries.

Number of allocations (approx.)	802
Bytes/Allocation (approx.)	2225.61
Total Bytes (approx.)	1784940
Memory leaks	
24 bytes (re-occurring at every main iteration)	*double maximum(double array[], int);* from *extraMath.h*
4 Kbytes (once at the creation of the bounding box)	*double maximum(double array[], int);* from *extraMath.h*
24 bytes (re-occurring at every main iteration)	*double minimum(double array[], int);* from *extraMath.h*
4 Kbytes (once at the creation of the bounding box)	*double minimum(double array[], int);* from *extraMath.h*

Table 5.1 Table showing the average number of bytes allocated and the memory leaks

One thing we mentioned before is the fact that computational geometry is quite different from analytic geometry. This has been particularly realised here, in the implementation stage, where because of small approximation errors, arithmetic operations produce unexpected results. Such occurrences where in the detection of connected components. This is carried out by comparing the sides of tri-

angles to see if they match and therefore form a mesh. At the beginning, when the object was complete, there is no problem with such comparisons, but when we cut and reconstruct the object, the new triangles might not fall exactly next to each other. This leads to detection of more connected components than normal. We therefore had to manually examine every vertex of every triangle of every identified connected component, to check for any degeneracies or triangles that were almost connected. From carrying out all this laborious checks, we managed to extract an appropriate threshold to counteract these computational geometry problems.

Similar such thresholds were introduced throughout different functions of the software, such as intersections and vertex comparisons, and as a result (because of the building-block approach of constructing our geometry) they are interdependent. What this means is that changing one threshold might cause another to fail, and by causing a chain-reaction effect, cause the system to produce the wrong results. We therefore had to find a balance between them, based on trial and error. We experimented with data, where we knew the results already, and adjusted the thresholds to get the expected output.

5.1.1 ALGORITHM COMPLEXITY

In this section we will present an estimation of the algorithm complexity as a way to characterise its efficiency. We have estimated the efficiency as the function $f(n)$ representing the maximum number of primitive operations required for an input of size n, and given in big-O notation. The approach we used for this estimation, was to consider the fundamental components of the system, approximate their individual complexities and then work upwards to get the overall algorithm complexity. Our methodology for complexity estimation is based around a qualitative approach proposed by [Che03], which has shown to lead to the final asymptotic complexity as the traditional formal analysis techniques do.

We considered the system as two distinct components, the affine erosion and the shocks detection. Estimating the complexity for the shocks detection was quite straightforward. It is $O(N^3)$, since we have to traverse the whole volumetric array and loop three times to access every chordal point.

However, since we already have the chordal points stored in lexicographic order, it is quite easy to convert to *O(N)* by using one iteration, but considering that even with $O(N^3)$ the skeletonisation process takes only a few seconds to complete, it was decided to keep the current solution.

The next part, the affine erosion, was the most difficult part of the system to estimate. We have identified the following processes as being the most significant for affecting the overall complexity. Their respective complexities are also shown:

- *bBox()*: generate a bounding box to enclose the volume. Complexity= *O(N)* where *N* is the number of triangles in the original object.
- *pointInPolyhedron()*: test a single point if it is inside a general polyhedron. Complexity= *O(N)* where *N* is the number of triangles in the original object.
- *generatePoints():* traverse the bounding box and generate points inside it at specific intervals Δt in all directions. While the points are being generated we use the point in polyhedron method to test for containment. Complexity= *O(KJLN)* where

  $K=\frac{Xbounds}{\Delta t}$, $J=\frac{Ybounds}{\Delta t}$, $L=\frac{Zbounds}{\Delta t}$ and *N* is the number of triangles in the original object. In the case that *Xbounds=Ybounds=Zbounds* (bounding cube) then the complexity becomes $O(M^3N)$. Note that this complexity contains the complexities of the two previous operations (*bBox()* and *pointInPolyhedron()*) and although necessary for the erosion, it can be implemented as a standalone program. It is even possible not include this function in our system all and read the pre-computed internal points from a file. Therefore, we will include this complexity as a separate entity, when we calculate the total complexity at the end.
- *CutNReconstruct():* cut the boundary by a plane and reconstruct only those that the plane intersects. Complexity= *O(N)* where *N* is the number of triangles in the original object.
- *FindAdjacent():* find the adjacent triangles of a given triangle in a boundary. Complexity= *O(N)* where *N* is the number of triangles in the original object.

- *FlagConnected():* recursive function that looks if a triangle has adjacent triangles, and if so sets their connected flag to true. Complexity= *O(N)* where *N* is the number of triangles in the original object.
- *GetConnected():* find the connected components in a given polyhedron.. Complexity = $O(N^2)$ where *N* is the number of triangles in the original object. Note that this function makes use of *FlagConnected()* and *FindAdjacent()* and so it includes their respective complexities.
- *pointInOpenPolyhedron():* similar function to *pointInPolyhedron()* that tests a single point for being inside a general, open polyhedron. Complexity= *O(N)* where *N* is the number of triangles in the original object.

Any operations such as assignment, comparison, multiplication, addition and so on, and any sequential combination of those where no iteration is involved (e.g. an intersection between a line and a triangle), have been estimated as having constant complexities of O(1) and therefore have been merged with linear, quadratic and cubic complexities, since $O(1) \subset O(N) \subset O(N^2)$ and so on.
Going back to the main function and considering all the above calculated complexities the final complexity will be:

$$\underset{generatePoints()}{O(M^3N)} + \underset{main\ loop}{O(N)}\left[\underset{while\ loop}{O(L)}\left[\underset{CutNReconstruct()}{O(N)} + \underset{GetConnected()}{O(N^2)} + \underset{for\ loop}{O(K)}\left(\underset{pointInOpenPolyhedron()}{O(N)} + \underset{for\ loop}{O(R)}\right) + \underset{for\ loop}{O(N)} + \underset{for\ loop}{O(S)}\right]\right]$$

where *N* is the number of triangles in the object, $L = \frac{\sqrt{(Xbounds\,\Delta t)^2 + (Ybounds\,\Delta t)^2 + (Zbounds\,\Delta t)^2}}{\Delta d}$,

Δt is the volume discretisation size, Δd is the distance we advance the plane in every iteration, *K* is the number of connected components, *R* is the number of chordal points *x'* inside the volume and *S* the number of re-entry points identified by our intersection test.

By doing the calculations and merging complexities we get:

$$O(M^3N) + O(N^3L) + O(LN^2RK) + O(NLS)$$

Remember the first term $O(M^3N)$ is the complexity of the *generatePoints()* function and we do not wish to merge this as we mentioned before. Now, considering that $2 < S << N$ because the re-entry points will never be as many as the number of triangles for a closed volume, we can say that $N^3L >$

NLS and merge the complexities. Furthermore, the number of connected components are usually between 1 and 10 and so much less than *N*, therefore $1<K<<N$ and we can simplify $O(LN^2RK)$ to $O(LN^2R)$ since we are not going to considerably affect its asymptotic behaviour. So we end up with $O(M^3N)+O(N^3L)+O(LN^2R)$. From here, we can safely assume that the number of chordal points for a normal execution of the program will be $R>>N$ and so $N^3< N^2R$. This means that $O(N^3L)$ can be merged with $O(LN^2R)$.

Taking this into account and introducing the shocks detection complexity we have:

1. generate internal points complexity: $O(M^3N)$
2. affine erosion: $O(LN^2R)$ which is approximately > $O(N^4)$
3. shocks detection: $O(N)$

These estimations are dependent on the following parameters. The number of triangles *N* in the original object, the number of chordal points *R* that we have generated (based on the dimensions of the object and the Δt discretisation parameter), the number of times *L* the cutting plane has to be advanced (based on object dimensions and Δd). So, to summarise, the two parameters the user inputs (Δt and Δd) together with the triangles of the object and its volume (dimensions) are what affect the complexity of the algorithm, which makes sense if we see how changing this values affect the execution time. It would be possible to further simplify these estimates, if instead of using Δt as a parameter and calculating the internal points from Δt and the dimensions of the object, we could pass the number of desired points as a parameter to the program. This would make the *M* and *R* parameters (above) obsolete, but unfortunately would require a redesign of some parts of the system.

5.2 STRESS TESTING

This testing strategy, relies on stressing the system by going beyond its specified limits and determining how well it can cope with overload situations. Normally, we have an estimation of the capabilities of the system at design time and we use stress testing to verify them. However in this case, because of the type of design and inherent complexity, it has proved difficult to make an accurate estimation of the capabilities of the system. We therefore, decided to use stress testing as a means of

exploring these capabilities and not so much to verify them.

Since we can only test the system as a whole, we have no choice but to make test cases by using the input parameters. These are the number of triangles in the object, the bounding box discretisation size Δt, the distance Δd that the cutting plane advances, and the dimensions of the object. We have been experimenting with very high or very low values of these parameters and managed to find some operational limits of our implementation. These are:

- *Number of triangles:* Having tested a variety of input objects with increasing triangle size, we can conclude that the implementation copes well with datasets of up to 21500 triangles. It will fail however, with data sets of 24000+ triangles and cease execution at the input file reading stage. This indicates that it probably exceeds the allowed memory size for storing a linked-list so a new approach is necessary that will store the data in other parts of memory or in the hard disk and access only portions of it at a time, instead of trying to read the whole chunk in one go. As far as minimum triangles are concerned, it can successfully cope with a tetrahedron ($N=4$) and even execute for ($N=3$), which is not a closed volume and the results will not be geometrically correct.

- *Dimensions of the object:*When the dimensions are very small from $minX= minY= minZ= 0$, to $maxX=maxY=maxZ=0.8$ then in order to get the program to work we haver to set Δt below 1. In that case the program appears to be working, but does not generate the internal points correctly. Although it calculates correctly the number of points it should create, it does actually not create them. This is because traversal in the volumetric array uses integer arithmetic (discretised) and cannot work when the dimensions and Δt are less than 1. As for very large dimensions, we experimented with a variety of different values and we have seen that for sufficiently large numbers ($>8 \cdot 10^7$) it affects the volume calculation, by generating negative numbers for volume approximations. This is a quite strange behaviour, the exact cause of which we cannot establish at the moment, but it may be related with the capacity of float-type variables being exceeded.

- *Δt:* We have tested the discretisation size with a variety of very high and very low values to determine how it can affect the system. Most notably, for extreme values, such as $\Delta t = \pm 10^{25}$ the program still executes successfully but has no practical meaning since the number of generated points will be zero (unless of course the object has dimensions in the order of 10^{25}). At even more extreme values (order of 10^{50}) we noticed the system was not iterating properly because the dimensions of the bounding box became undefined. This is most probably associated with the the storage capacity of a double precision floating-point variable being exceeded. For $\Delta t = 0$ the program goes into a never ending loop.

- *Δd:* Finally, we tested the distance the plane advanced at every iteration. The results seemed quite promising, since for very high values (negative and positive are the same, the only thing that changes is the direction in which the plane travels (upwards or downwards). For $\Delta d = 0$, the the program worked normally, although without any practical meaning since the plane was outside of the object, did not move and there were no chordal volumes defined.

So now we can say that we have a better understanding of what the operational limits of our software are. It would be quite possible at this stage to either adjust the program so that when in a stress situation like above, to degrade gracefully instead of just crashing and perhaps corrupting the data. An alternative would be to make the user aware of these operational limits, and ensure the input data and passed parameters, are within the limits we have identified.

The detailed tests for each of the above cases can be found at the appendices.

6 EXPERIMENTS AND RESULTS

This chapter contains a summary of the different experiments we run with our skeletonisation software, both on artificial and real 3d data (human body scans). Details of such experiments, such as the parameters chosen and the execution time, together with their results are also presented. These results are compared with other skeletonisation methods, such as the 3d medial axis and the 3d affine skeleton approximation by Jeong and Buxton [JB01] We go on to discuss whether or not the skeletons produced by our software are indeed affine invariant and noise resistant. We conclude this chapter with a discussion on the limitations of our algorithm.

6.1 ARTIFICIAL DATA

We chose to experiment with artificial data obtained by Joao Oliveira [OJ03] or generated in freely available software [W3D03]. This data was a variety of triangulated primitive objects with manifold meshes in OFF format. We used such data primarily for its simplicity while we were developing and testing the software, but also to determine how the affine skeleton can compare with the medial axis, since the medial axis has already being studied in primitive 3d shapes.

Our first example, which can be seen on the left of Figure 6.1 is a triangulated torus with 256 triangles. Our skeletonisation program produces the affine skeleton (second image from the left). As we can see its a 2d flat surface, which is similar to the results of the medial axis transform on a 3d object. That is, the medial axis of a 3d object will be a surface, apart from rare cases where degeneracies are produced. Nevertheless, it is interesting to see the results of popular 3d medial axis approximation software, such as [ACK01] and [DG03], that we mentioned in chapter 2 above. The second picture from the right is the result from *Tight-Cocone* and the rightmost picture is the result of medial axis approximation with *Powercrust*. Although *Powercrust* cannot produce a connected skeleton in this case, we can clearly see that both software try to produce a 1-dimensional skeleton. We would like to emphasise the fact that these software do not follow the theory for calculation of the 3d medial axis but only provide an approximation of it. What this means is that there is a possibility that the approximated medial axis is 1-dimensional, unlike the affine skeleton that is always a

surface in 2 dimensions. It might be desirable in certain application areas, such as animation and object matching, to have 1-dimensional skeletons, but from a theoretical point of view, the skeletons produced by *Powercrust* and *Tight-Cocone* are not very interesting.

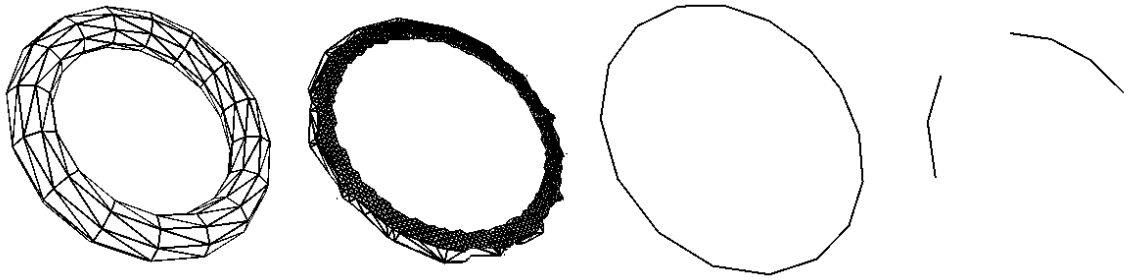

Figure 6.1 (Left) A triangulated torus, (second from left) its affine skeleton, (second from right) medial axis approximated by *Tight-Cocone* and (right) medial axis approximated by *PowerCrust.*

Our next example, takes the same torus and performs a local deformation such that, it reduces the width of one side of the torus (Figure 6.2 leftmost image). We apply the same algorithm to get the affine skeleton (second from the left). We can see now that the affine skeleton becomes disconnected. This is not surprising because we know that the affine erosion erodes the object in a uniform way, removing all the chordal points with erosion level-set function $E(x,V)$ bellow a certain threshold. It is therefore expected that points in thin parts of the deformed torus may be completely removed since all the points inside these areas will have $E(x,V)<threshold$. The skeleton will reflect this behaviour with discontinuities. We can also see the results of *Tight-Cocone* and *Powercrust* (second from the right and rightmost images respectively) when trying to approximate the medial axis. *Powercrust* still produces large discontinuities in the boundary of the medial axis, unlike the *Tight-Cocone* that produces a closed skeleton.

What is interesting to note here, is that the deformation of the torus, produced some surfaces in the medial axes approximations by *Powercrust* and *Tight-Cocone*. What is even more striking is that these surfaces appear in places where before there used to be a 1-dimensional centreline (Figure 6.1 two rightmost images), even though the thickness of the torus remains the same in both cases. We can assume therefore, that by locally deforming a shape, we might affect the medial axis in other areas, not affected by this deformation. This strange property is not exhibited by the the affine skel-

eton, which is a 2d surface throughout.

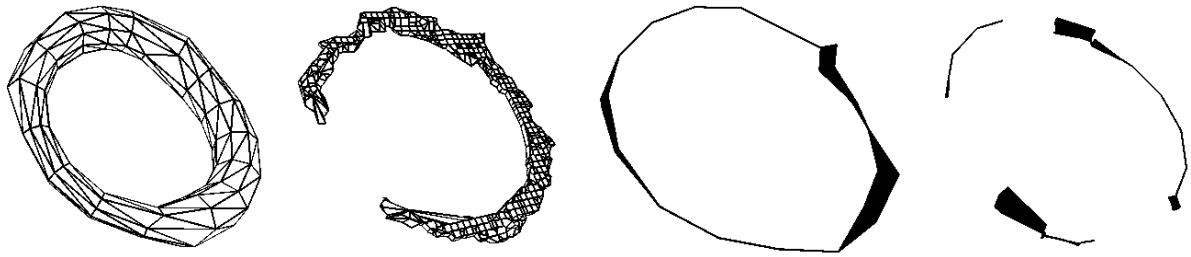

Figure 6.2 (Left) A torus with a local deformation at one side, (second from left) its affine skeleton, (second from right) medial axis approximated by *Tight-Cocone* and (right) medial axis approximated by *PowerCrust.*

Our next result is from an experiment on a ellipsoid object. In their work, Betelu et al. [Bet00], have shown that the affine skeleton of en ellipse (the 2d equivalent of an ellipsoid) is a line, whose length depends on the length of the major axis of the ellipse. An ellipse can also be thought of as a circle that has been elongated by affine transformation. By virtue of the affine invariance property of the affine skeleton, the skeleton of the circle (its centre) will be elongated via the same transformation, giving a line in the centre of the ellipse . This idea can be seen in Figure 6.3. Now that we know that the skeleton of an ellipse is a 1-dimensional line, we can expected that the affine skeleton of an ellipsoid in 3d, will be a rectangular surface, since this is the equivalent of a line in 3 dimensions.

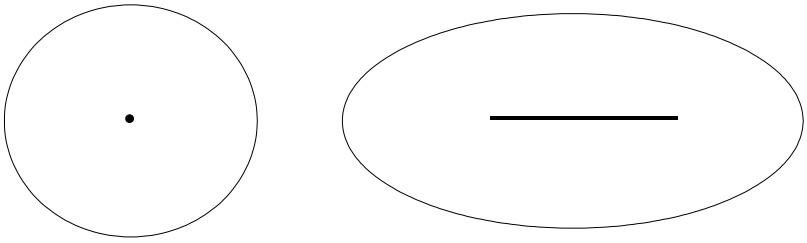

Figure 6.3 The affine skeleton of a circle an that of an ellipse

As we can see in Figure 6.4, this happens to be the case, and the affine skeleton of an ellipsoid is a 2d rectangle (middle picture). The dimensions of this rectangle are dependent on the dimensions of the axes of the ellipsoid. We also tried to calculate the medial axis of the ellipsoid with *Powercrust* and *Tight-Cocone. Powercrust* did not produce any results, unlike *Tight-Cocone*, which produced a 2d planar surface (right picture) similar to but not as well defined as the affine skeleton. There

seem to be more jugged edges in the medial axis approximation, probably related with either surface noise or the low resolution of the ellipsoid. In this case, the medial axis as approximated by *Tight-Cocone* is a surface suggesting that there is no consistency between the dimensions of skeletons of different 3d objects. The affine skeleton on the other hand seems to be more consistent and always produce a 2d surface. This of course is not a proven fact but our opinion which is based on our results.

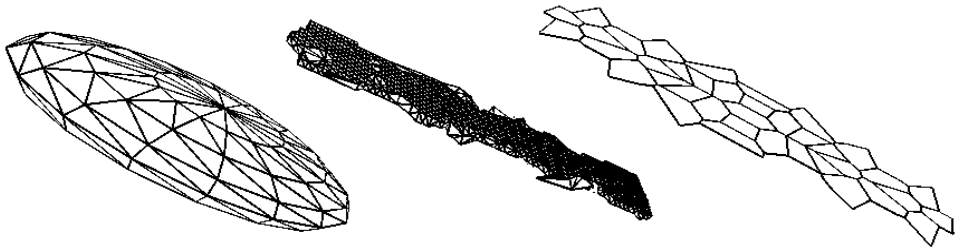

Figure 6.4 On the left a triangulated ellipsoid and its affine skeleton (middle). On the right we see an approximation of its medial axis by the *Tight-Cocone* software.

Now we examine a case where our skeletonisation algorithm will produce a degenerate surface. This is the special case of the sphere. We know that the affine skeleton of a circle in 2d is its centre (Figure 6.3), similar to the 2d medial axis of a circle which is its centre by definition. In 3d dimensions, the affine skeleton of the sphere, is a cluster of points approximately in the centre of the sphere (Figure 6.5 middle image). This is because the erosion of a sphere will always be a sphere with a diminishing radius. As the sphere erodes, this cluster of points will always be equidistant from every point in the boundary (by distance here we mean the volume of the chordal set as defined in chapter 3) and therefore they will be points in the affine skeleton. In terms of shocks, these can be though of as fourth-order shock points, which are generated when a closed boundary collapses under erosion into a single point. We have a cluster instead of a single point, due to the difficulty identifying such higher-order shocks in computational geometry, as we have mentioned in chapter 3 previously. When we tried to approximate the medial axis as before, we got this strange linear skeleton from *Tight-Cocone* (Figure 6.5 right image), while *Powercrust* could not approximate the medial axis of our sphere at all. We have to admit that we could not explain why these very popular medial axis approximation software produced these results.

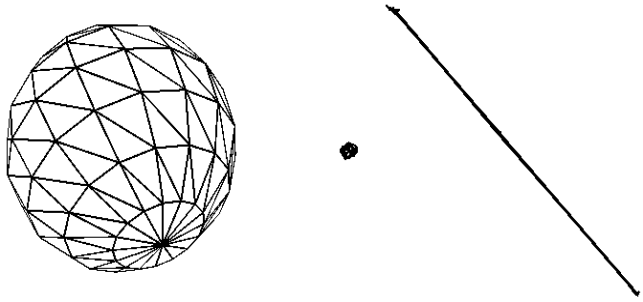

Figure 6.5 A sphere (left) and its degenerate affine skeleton in the middle. On the left the strange linear skeleton produced by *Tight-Cocone*.

For our final experiment with primitive shapes, we calculated the affine skeletons of a cylinder and of a cone (Figures 6.6 and 6.7 respectively). The affine skeleton of the cylinder (Figure 6.6 on the right) resembles an hourglass shape. Intuitively, this resembles the medial axis of a rectangle (see Figure 1.1 in page 5) that has been rotated about its major axis. If we assume that the equivalent of a cylinder in 2d is a rectangle and that we can go from a rectangle to a cylinder simply by rotation along its major axis, then our results of the 3d affine skeleton seem to be consistent with the 2d case. Moving on to Figure 6.7, we have computed the skeleton of a cone. If we think of a cone as a cylinder with one side collapsed into a single point, then we see that its affine skeleton (Figure 6.7 right image) resembles the affine skeleton of the cylinder (Figure 6.6 right image) if one of its side is collapsed into a point. We can therefore say, that the affine skeleton will retain the topological properties that exist between similar classes of primitive objects.

We should perhaps mention that neither *Powercrust* nor *Tight-Cocone* could approximate the medial axes of the our cylinder and cone.

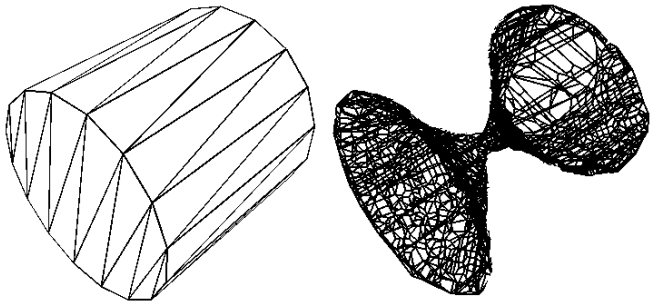

Figure 6.6 A cylinder (left) and its affine skeleton (right)

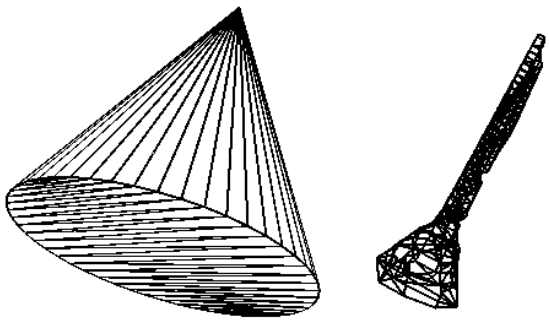

Figure 6.7 A cone and its affine skeleton (right)

6.2 REAL DATA

We will now apply our skeletonisation algorithm to real data, captured by the Body Lines scanner [Hor95] available at the computing department in UCL. These are triangulated 3d scans of human bodies at different resolutions (i.e. number of triangles). A small sample can be seen in Figure 6.8.

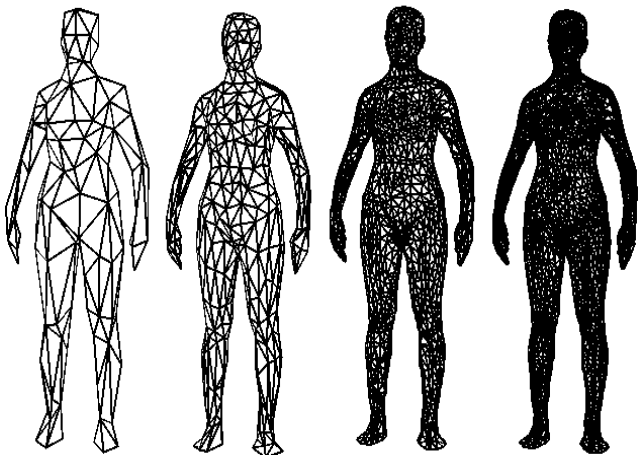

Figure 6.8 Human bodies in different resolutions. From left to right: with 292, 500, 1000 and 5000 triangles respectively

The first results of applying the 3d affine skeleton to human body scans can be seen in Figure 6.10. This is the skeleton from a low resolution triangulated body with 292 triangles. The first results are far from perfect, but seem quite promising. We can see a front view of the skeleton (Figure 6.10 left image) and a side view (Figure 6.10 right image) that clearly illustrates that the skeleton is 2-dimensional, consistent with the results we produced in the previous section. The biggest visible problem

with this skeleton is that it contains numerous discontinuities.

Figure 6.9 The affine skeleton of a 500 triangle human body.

We believe that these discontinuities are caused by both a practical an
theoretical of course is the computation of shocks as we have mention
report. The practical problem is the parameters with which the progra
is section 5.1.1 the complexity of the algorithm depends on the three
angles N in the body, the volumetric array discretisation size Δt and t
travels with every iteration. The higher the number of triangles and lo
the program will take to execute. To produce the results in Figure 6.1
relatively low number for Δt and
respectively). We did this to save computation time, because as we w
process can take a very long time to finish.

The drawback of using low resolution objects with such high values for Δt and Δd, is that the approximation of chordal volumes via linear interpolation (see section 3.2.1) will be very crude, and so will be the computation of the skeleton. In addition, because an object with a high number of triangles approximates volume much better than an object with a few triangles, volume computations (which are fundamental processes in 3d affine erosion) will be much more accurate when N is large. Finally, the more triangles, the more cutting planes will be generated at different orientations. This means that we will sample the chordal points closer to the theoretically large number of orientations necessary to compute the erosion level-set function $E(x,V)$.

To prove this, we have executed the program with a 500 triangle model and $\Delta t=\Delta d$=200 pixels, and calculated its affine skeleton. The results can be seen in Figure 6.9. Not that a 500 triangle model can be defined as high resolution, but still the improvement from the skeleton in Figure 6.10 is significant. Straight away, we see that the connectivity of the skeleton points has been improved, especially in the torso, head and shoulders area. This slight increase in resolution brought about a substantial increase in execution time. Whereas the first the 292 triangle model in Figure 6.10 took approximately 35 min 41 sec to execute, the 500 triangle model in Figure 6.9 took in excess of 1 hour and 45min to complete. This is more than a threefold increase in execution time for a 2.5 increase in

surface triangles. The gap between resolution increase and execution time increases as we increase the number of triangles *N*. We will see more details of this later on.

6.2.1 TRIANGULATION

We should mention here once again that the output of our algorithm is a point cloud (i.e. disconnected points in 3d space). The medial axis approximation software that we have seen above (*Powercrust* and *Tight-Cocone*) produce a triangulated surface by computing the convex hull of the object. This might produce acceptable results for convex objects, but for complex non-convex objects such as human body scans the triangulated surface is not very accurate. We have used a different technique (although not implemented as a requirement of this project) called the 3d α-shape [EM94]. Alpha shapes can be thought of as generalizations of the convex hull of a point set, where by varying a parameter (called alpha), we can get shapes ranging from crude to fine. The most crude shape is the convex hull itself, which can be obtained when alpha is very large. As alpha decreases, the shape shrinks and develops cavities that may join to form tunnels and voids. These cavities are what we are interested in, because they are very common in complex objects such as human models (e.g. cavities under the arms and between the legs). The results of α-shape triangulation in the skeleton from Figure 6.10 can be seen in Figure 6.11. The skeleton which now is a triangulated surface, looks more complete, with fewer discontinuities.

The problem with the α-shape approach, is that because it depends on the right choice of the alpha parameter, and this parameter is difficult to find, most of the times constructing the triangulation of the boundary of a shape requires trial and error. An alternative to α-shape is the marching cubes [LC87] but will not work sufficiently if there are many disconnected points or boundary noise.

Figure 6.10 Affine skeleton of a 292 triangle human body. (left) front and (right) side view.

Figure 6.11 The same skeleton that has been triangulated .

6.2.2 MEAN CURVATURE THRESHOLD

As we have already mentioned, in order to find the shock points in $E(x,V)=constant$ we need to select those points where the mean curvature is greater than a fixed threshold τ. Betelu et al. [Bet01] have proposed that this threshold is in the order of the inverse of the discretisation size of the volumetric array (see section 3.2.2). We have tried this approach and found it to be appropriate when we used the intermediate difference operator to compute the divergence $\nabla.n(x)$ of the optimal chord normals. However, when using the Zucker-Hummel gradient operator, the same threshold does not apply. We therefore used trial and error to find another τ that produced a good approximation of the 3d affine skeleton. Figure 6.12 shows how the approximated skeleton is affected by different choices for τ. After trying a variety of thresholds, we came to the conclusion that for $\tau=7$ we get the most eye-pleasing results. We are not sure what the significance of this number is, and how it is related with the choices of parameters Δt and Δd, but we found it to be consistent among all experiments we carried out with real and artificial data (see section 6.1), and always produced the best results.

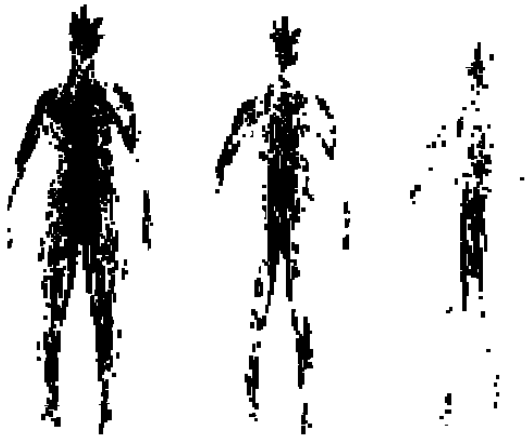

Figure 6.12 The affine skeleton of a 292 triangle body, for different thresholds τ (from left to right) τ=9, τ=7, τ=6

6.2.3 COMPARISON WITH OTHER METHODS

We have also computed an approximation of the medial axis skeleton by using the *Tight-Cocone* and *Powercrust* programs, in order to compare them with our affine skeletons. Initially we used the same 292 triangles body model (Figure 6.8 leftmost image). Surprisingly, *Tight-Cocone* could not produce any results whatsoever, whereas *Powercrust* produced the leftmost skeleton in Figure 6.13. Compared with our results in Figure 6.11, it is straightforward to see that our algorithm performs much better with lower resolution models, producing a skeleton that still resembles the topology of the human body. When we used a higher resolution model with 500 triangles (Figure 6.8 second image from the left) both the *Powercrust* and *Tight-Cocone* produced much better results with very good connectivity (Figure 6.13 middle and right images respectively). When compared with the affine skeleton of the same 500 triangle body in Figure 6.9 it is clear that the skeletons from *Powercrust* and *Tight-Cocone* perform much better as the number of triangles increases.

Note however, that the skeletons in Figure 6.13 are triangulated whereas ours is not, and furthermore, *Powercrust* and *Tight-Cocone* are specifically built and adjusted to produce eye-pleasing medial axis skeletons. These skeletons are subjected to a variety of enhancing procedures (such as noise removal) and do not necessarily follow the extension of Blum's [Blu64] medial axis theory in 3d (i.e. using maximal spheres to detect skeleton points). This becomes more apparent if we do a

comparison between the *Powercrust* and *Tight-Cocone* skeletons. Even though they should represent the same skeletonisation method and in theory should look similar, they do not. Note the significant differences between the hip and head regions in the middle and right skeletons of Figure 6.13.

Finally, we would like to make a visual comparison of our affine invariant skeleton, with the one by M.S.Jeong and B.Buxton [JB01]. Their method is based on computing the 2d affine invariant skeletons of horizontal slices of the human body and bringing them together to form an approximation of the 3d affine invariant skeleton. Such a skeleton can be seen in Figure 6.14. This skeleton has been produced form a high resolution human body scan, much more detailed than our example in Figure 6.8, in and so it exhibits very good connectivity. The 3d skeleton that is produced by means of 2d skeletonisation, has different geometrical properties from our 3d affine skeleton. If we look at the left skeleton picture in Figure 6.14, we can see that the skeleton parts of the head, arms and legs have approximately the same thickness. This clearly does not correspond to the original human body model, where the head is much ticker than the limbs. Our skeletonisation method produces a skeleton (Figure 6.11) with areas of variable thickness that correspond to the parts where the original body is thick respectively.

In addition, note that the arms and (if we examine very closely) the legs are disconnected from the body. This is because of the limitation of their method, which can only deal with one connected component at a time. Cutting a horizontal slice at the torso will produce three connected components, which will be the closed curves formed by the intersection of the object's vertices and the cutting plane, and will correspond to the two arms and the torso. The 2d affine invariant skeleton cannot cope with more than one curves at a time, and so, applying such a method in a 3d non-convex objects will require the segmentation of the object into separate connected components (for a human body, the torso with the head, and the limbs). This segmentation process is not easy or unique, since a human body can be captured in many different orientations and positions, and will require manual intervention. In that sense, our algorithm is superior to that proposed by M.S.Jeong and B.Buxton [JB01], since it can cope with any amount of connected components without the need for manual intervention, provided of course we are applying the algorithm at one object at a time.

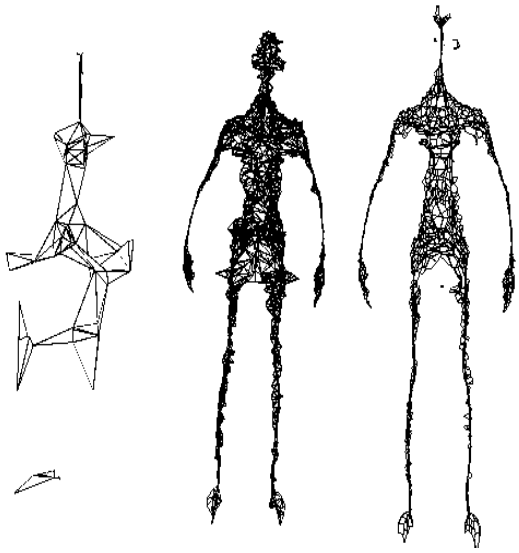

Figure 6.13 The medial axis of a 292 triangle model produced by *Powercrust* (left), the medial axis of a 500 triangle model by *Powercrust*(middle) and the medial axis from the same model by *TightCocone* (right).

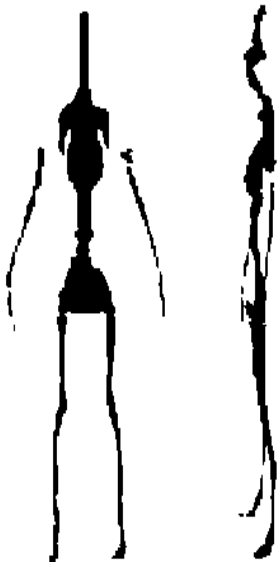

Figure 6.14 3d affine skeleton approximation by 2d cross-sectional slices

6.3 NOISE RESISTANCE

We will now see how robust the 3d affine skeleton is when noise is added to the boundary of the original object. We started by adding noise to a triangulated human model by randomly moving the surface vertices (i.e. multiplication of every vertex with a random value) and got the resulting noisy body in Figure 6.15 on the right. The noise values where chosen from a normal distribution with mean zero, variance one and standard deviation one.

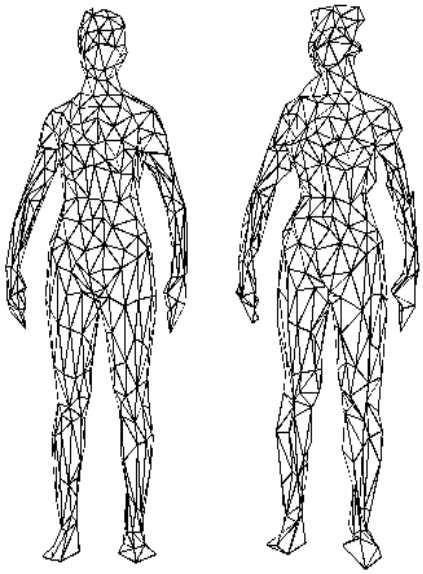

Figure 6.15 The original human body (left) and after random noise (right)

Figure 6.16 The affine skeleton of the original body (left) and the affine skeleton of the noisy body (right)

We then had to establish the similarity between the affine skeleton of the original body (Figure 6.15 on the left) and the affine skeleton of the body with surface noise (Figure 6.15 on the right). To do this, we compared every vertex from the first skeleton, with every vertex from the second. This comparison was carried out by computing the distance between the two vertices, and check to see if it was below a chosen threshold. If the squared distance was lower than the threshold, we flagged these points as being similar. In the end, we calculated the number of all similar points between the two skeletons, and if they were above a threshold we could then assume that the two skeletons were similar, and therefore conclude that the affine skeleton is not (considerably) affected by surface noise.

We have carried out a number of similarity comparisons, by increasing the square distance threshold. The similarity graph of the two skeletons from Figure 6.16 above, can be seen in Figure 6.17. Considering that these skeletons have approximately 5000 points each, according to the graph, a square distance threshold of 10^8 will give us approximately 94% similarity match.

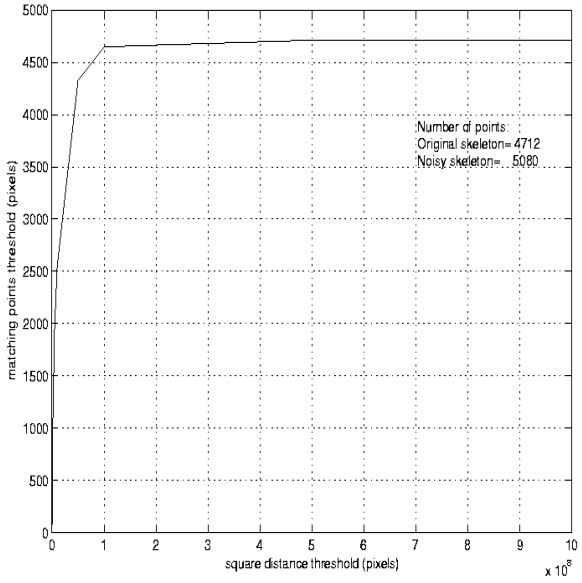

Figure 6.17 Graph plot of the number of similar points between the two affine skeletons, in relation to the square distance threshold.

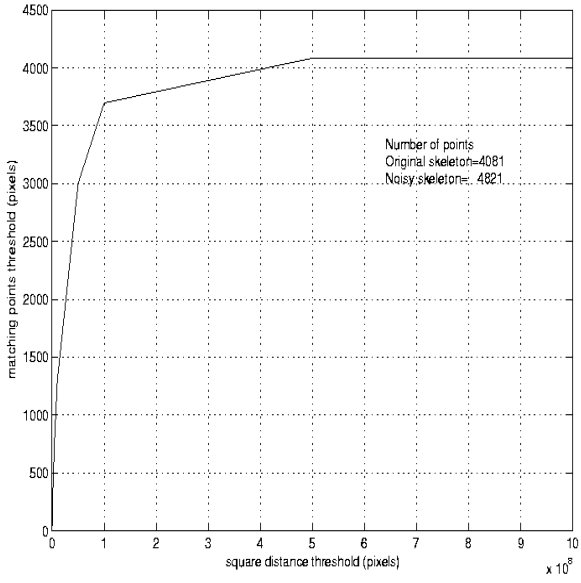

Figure 6.18 The similarity graph plot for the original and noisy skeletons, as computed by *Powercrust.*

However, we are not quite sure what would constitute an appropriate threshold. One way that we could devise a threshold, would be to consider the volumetric array discretisation size Δt. We have computed these skeletons, with a discretisation size of Δt=200 pixels, so the square distance of the major diagonal of a voxel will be $1.2 \cdot 10^5$ pixels. Perhaps we could use this value to determine an appropriate size for the threshold. Also before we can make any conclusions as to if the skeleton is noise resistant, we should decide on what constitutes an appropriate percentage for similarity matches, such as the area under the curve.

We have run the same noise resistance experiment by using the 3d medial axis as approximated by *Powercrust*, with exactly the same parameters (random noise amount and triangles in the body's surface). The resulting similarity curve, is drawn in Figure 6.18. We can see that for medial axis skeletons of approximately 5000 points each, a square distance threshold of 10^8 will give us less than 90% similarity match. This similarity mismatch can also be inferred from the area under the curve, which in Figure 6.18 is smaller than the area under the curve in Figure 6.17. We cant therefore conclude, that the 3d affine invariant skeleton computed by our algorithm, is more resistant to the same amount of surface noise, than the medial axis approximated by *Powercrust.* This observation is consistent with the theory behind the affine skeleton and the medial axis.

6.4 AFFINE INVARIANCE

The next step, is to determine if the affine skeleton is indeed invariant to affine transformations (see section 2.2). We first deform a human body scan with an affine transformation. We compose this transformation as a sequence of a rotation, a translation and a shear about an arbitrary axis of the body. The results of this affine transformation can be seen in Figure 6.19. The next step is to compute the affine skeleton of the original body (Figure 6.19 on the left) and subject it to the same affine transformation we subjected the body on Figure 6.19 on the right. Next, we compute the affine skeleton of the affine transformed body, and compare it with the transformed skeleton of the original body we computed before (Figure 6.20). The comparison process is similar to the one in the previous section when we compared the skeletons to determine the noise resistance property. The similarity graph between the compared skeletons from Figure 6.20 can be seen in Figure 6.21.

From the graph, we can see that there is a great similarity between the two skeletons, so for example like before, for skeletons of approximately 5000 points each, a square distance threshold of 10^8 will give us an approximate 98% similarity match. However, before we can decide if the affine skeleton is indeed affine invariant, we have to consider how these thresholds can be interpreted, as we have seen in the noise resistance test from section 6.3 above.

When we attempted the same experiment with the medial axis, *Powercrust* produced a medial axis from the affine transformed body, that was completely different from the affine transformed medial axis of the original body. More specifically, the affine transformed medial axis of the original body was contained 4821 pixels, whereas the medial axis from the affine transformed body contained only 373 pixels. A arithmetic comparison like before was not possible but even the fact that the two skeletons are so different in terms of size proves that the medial axis as approximated by *Powercrust* is not affine invariant.

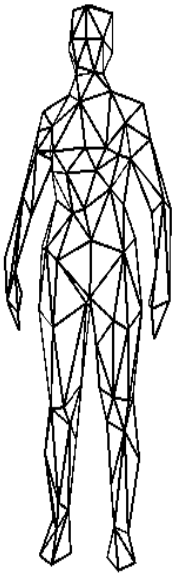

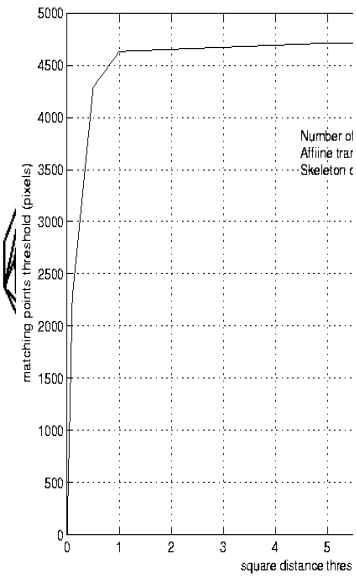

Figure 6.19 The or (left) and its affine tion (right).

Figure 6.21 The similarity gra ison of the two skeletons.

Figure 6.20 The affine transformed skeleton of the original body (left) and the affine skeleton of the body deformed by the same affine transformation (right).

6.5 LIMITATIONS

Although our algorithm can produce reasonable approximation to the 3d affine skeleton, it has some limitations. Apart from the accurate calculation of shock points, it is limited by the number of triangles *N* in the boundary of an object. This is a twofold problem, since a very small number of triangles (and subsequently a small number of possible orientations of the triangle normals) will not sufficiently sample all the orientations of the unit sphere, which as we know are necessary for accurate approximation of the erosion level-set function. On the other hand, a very large number of triangles (over 5000) will bring about an unusually large increase in the execution time of the program. In the next two sections we will examine these limitations in more detail.

6.5.1 CUTTING PLANES

The main goal of the 3d affine erosion is to calculate the greatest lower bound of the volume of all chord sets defined by all chordal points *x* inside a 3d object. In analytic geometry, this lower bound

is computed by rotating a cutting plane Π, defined on x in all the possible orientations of the sphere. In computational geometry, this solution is not feasible, so we have resulted in using the inward normals of the object's boundary as an alternative, hoping that they have a sufficiently large variety of orientations that can approximate the possible orientations of a sphere.

The algorithm that we described in chapter 3, in its current form, cannot cope with shapes where the number of triangles is very small and have little variety in the orientations of their normals. Therefore the computation of the 3d affine erosion for primitive objects such as a cube or a tetrahedron will not be accurate. Betelu et al. [Bet01] have proposed the introduction of more cutting planes when we are dealing with objects with little orientation variety of boundary triangle normals. They used a Monte Carlo technique to create random orientations and use them to rotate the cutting plane about a chordal point x. This method introduces a richer distribution of the normals to sample the object. When the number of triangles on the surface is sufficiently large, then the effect of the Monte Carlo technique is not noticeable.

We would like to propose a different method for introducing additional normal orientations, which is much faster and easier to control and configure than random ray generation. Our idea involves enclosing the object in a triangulated sphere, centred about the centre of gravity of the object and with radius equal to the major diagonal of the object's bounding box Figure 6.22. We will then use the inwards facing normals of the boundary triangles of the sphere as orientations for the cutting planes, while ignoring the triangles of the actual enclosed object. Since all the inwards facing normals will point towards the centre of the sphere, this method can guarantee a good sampling density independent of the number of triangles in the object, but only on the triangles of the sphere. The more triangles on the boundary of the sphere the better our sampling rate is. Even though this method cannot provide a solution for computing the affine erosion that is completely independent of the number of triangles in the object (only the generation of cutting planes will be independent, whereas the object's triangles are used in other processes such as chordal volumes computation and containment testing) it can reduce the overall complexity of the algorithm.

Apart from that, it has other desirable properties. By using the bounding sphere, the problems we

have seen in section 3.1 of the ever-advancing plane in complex shapes can be avoided by stopping the plane when it exits the radius of the sphere. In addition, it is quite easy to adjust the number of triangles on the sphere's boundary and thus adjusting the complexity of the algorithm. Note, that it was not possible to do that before by adjusting the number of triangles on the given object. With this method we have better control on almost all of the parameters of the algorithm (see section 5.1.1. for parameters that affect the algorithm complexity).

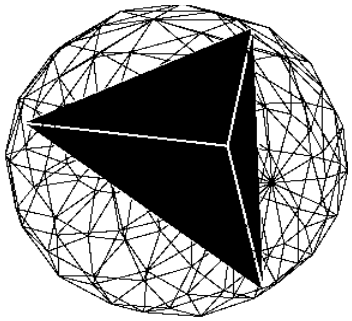

Figure 6.22 A bounding sphere that encloses a tetrahedron as an attempt to introduce a richer variety of normal orientations.

6.5.2 EXECUTION TIME

In the opposite case, when there is a large number of triangles *N* in the boundary of the object, the execution of the program will be severely affected, with an increase in the overall complexity. We have carried out a number of test runs of the skeletonisation program, where we have kept every parameter constant, while varying only the number of triangles. We did this to determine how a change in the number of triangles will affect the execution time and to what extend. The results can bee seen in Figure 6.23.

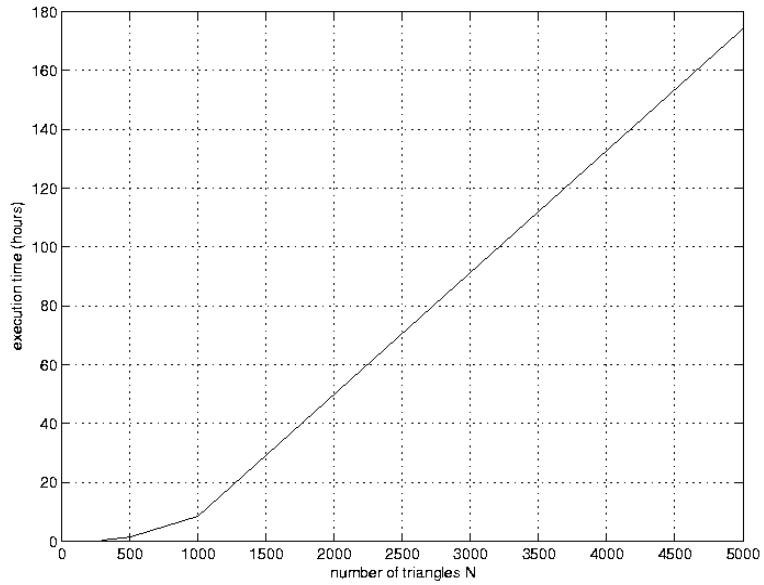

Figure 6.23 Graph plot of how the execution time is affected by the number of triangles

We can see that the execution time increases geometrically as the number of triangles is increased. Note that the reason why the graph might appear as linear at the end, is because after 1500 triangles, we had to extrapolate the data, based on preliminary results. It was simply not possible to wait in excess of 180 hours for a 5000 triangle model to complete. The results where carried out on a dual Celeron 550 Mhz PC with 194MBytes of RAM.

7 CONCLUSION

This is the final chapter of our report and it contains the summary of our work so far and the overall conclusions. In addition to that, we discuss certain ideas about possible future work on how to improve the 3d affine invariant algorithm, and possible application areas and extensions.

7.1 SUMMARY

Starting by reviewing our experiments and results from the previous chapters, we could say that we have gained a better idea of how the affine invariant skeleton looks in a variety of different objects. This is quite important because this is the first time the 3d affine invariant skeleton has been subjected to such rigorous testing with a variety of data. We have established that, for 3d objects the affine skeleton will be a 2d surface in similar way to the 3d medial axis skeleton. The exception to this rule are a few 3d objects whose skeleton will contain degenerate surfaces, such as the sphere.

The 3d affine invariant skeleton, is fundamentally different from skeletons produced by other skeletonisation methods such as the Reeb graph, which produces 1-dimensional skeletons. This property of the affine skeleton, does not make it very good for applications such as object recognition and tracking and animation of articulated objects. It is however possible to use this kind of skeleton as a starting point for surface reconstruction, similar to the inverse medial axis transform. The only problem is that so far a definition for the inverse of the 3d affine invariant erosion (e.g. the 3d affine dilation) does not exist. Unlike the medial axis transform where we could completely recreate the surface by means of the skeleton and its distance transform, such an approach for reconstructing surfaces with the use of the affine skeleton may not be possible.

We have also examined the appearance of the 3d affine skeleton when computed from 3d human body scans, and compared our results with other skeletonisation methods. Those skeletons we used for comparisons where computed by popular software, such as the *Powercrust* and the *Tight-Cocone.*

We also proved by experiments that the fundamental properties of the affine skeleton, which are noise resistance and invariance under affine transformations, indeed extend to 3 dimensions. We have shown this, not simply by using an intuitive approach such as the way the skeleton looks, but based on detailed arithmetic calculations and comparisons.

We have estimated an overall complexity of our algorithm and seen how the number of triangles can affect the execution time, which grows geometrically as the number of triangles increases.

This project is a continuation and extension to research previously undertaken in the computing department of UCL by M.S.Jeong and B.Buxton [JB01]. Their algorithm required manual intervention for segmentation and also requires that the human body was given in appropriate sliced format. We managed to build robust software, that can be used instead, with improved results, without manual intervention and more importantly able to work with more conventional formats [Geom] and data that is more similar to the one produced by the Body Lines 3d scanner available at the department.

If we consider the fact that our algorithm does not include any additional stages for noise removal, connectivity adjustments or generally any procedures that aim to improve the appearance of the resulting skeleton, we can claim that our implementation, is a pure approximation of the affine invariant skeleton in computational geometry and closely follows the theory proposed by Betelu et al. [Bet01]. From this point of view, the skeletons our algorithm produces have potential theoretical interest from research into surface evolution, shock generation and detection and the effects of 3d affine erosion. On the other hand, it is always possible to add any improvements similar to what other popular skeletonisation algorithms have. We can do so if there is a need to generate affine invariant skeletons that have more practical use.

7.2 FURTHER WORK

There is a lot of potential for future work in the subject of 3d affine skeletons. The biggest challenge would be to further reduce the computation time of the algorithm. We have given some ideas

throughout this project than can reduce its running time, but there is still a long way to go before this skeletonisation method becomes practically useful.

The next area where there is room for improvement, is the computation of shock points. We have used a basic method for computing these singular points but lately, there have been alternative approaches [SK96] , [Sid99] for better approximation of shocks that if incorporated to our algorithm may produce better results.

Also some of the issues that we did not manage to address in this project, is whether or not the affine skeleton is affected by re-mesh and mesh simplification processes on the original object. The results of such processes could be manifested as discontinuities on the skeleton, something we have experienced with human bodies of different resolutions (i.e. that have been simplified to get to a representation with fewer triangles), but were not able to test and prove accurately. Finally, there is always the possibility of surface reconstruction with the use of the 3d affine skeleton. Research could be carried out on ways to go from the skeleton to the original surface, via the inverse of the 3d erosion. Furthermore, because of the amount of time our algorithm takes to execute, we did not have a chance to fully experiment on more detailed human body scans. As a result, we could not fully appreciate the properties and appearance of the affine invariant skeleton. It would be an interesting extension to experiment on bodies with higher resolutions.

Since the beginning of our project, we have seen some very interesting new approaches on how to compute skeletons and also alternative solutions for the computation of the 3d affine invariant skeleton, that might produce more eye pleasing skeletons. We still believe however, that the 3d affine invariant skeleton based on the affine erosion, has some inherent properties that distinguish it from other skeletons in other application areas. We are confident that even though practical application for this type of skeleton might not be very obvious, with the necessary research it is possible to get over the major shortcomings of this method. Research is never in vain and should be carried out even when a subject might appear to have little practical use.

REFERENCES

[ACK01] N.Amenta, S.Choi and R.Kolluri, "*The Power Crust*", Proceedings of the sixth ACM Symposium on Solid Modelling and Applications, pp.249-260, 2001

[Ame02] N.Amenta et al, "*A simple algorithm for homeomorphic surface reconstruction*", International Journal of Comp. Geom. & Applications, pp.125-141, 2002

[AW02] M.Ahmed and R.Ward , "*A Rotation Invariant Rule-Based Thinning Algorithm for Character Recognition*", IEEE Transactions on Pattern Analysis and Machine Intelligence, pp.1672-1678, 2002

[Bet00] Betelu S., Sapiro G., Tannenbaum A., Giblin P., "*Noise-resistant affine skeletons of planar curves*", ECCV 2000, pp.742-754, 2000

[Bet01] Betelu S., Sapiro G., Tannenbaum A., "*Affine invariant erosion of 3d shapes*", Proceedings of the Eighth International Conference On Computer Vision, pp.174-180, 2001

[BKS01] I.Bitter, A.Kaufman and M.Sato, "*Penalized-distance volumetric skeleton algorithm*", IEEE Transactions on Visualization and Computer Graphics, pp.195-206, 2001

[Blu64] H. Blum, "*A transformation for extracting new descriptions of shape*", Symposium on Models for the Perception of speech and Visual form, pp., 1964

[Blu73] H. Blum, "*Biological shape and visual science*", Journal of Theoretical Biology, pp., 1973

[BP01] G.Barequet and S.Hal-Peled, "*Efficiently approximating the minimum-volume bounding box of a point set in 3 dimensions*", Proc. 10th ACM-SIAM Sympos. Discrete Algorithms, pp.82-91, 2001

[Ca86] J. Canny, "*A Computational Approach to Edge Detection*", IEEE Transactions on Pattern Analysis and Machine Intelligence, Vol. 8, No. 6, pp.n/a, 1986

[Che03] S.Y.Chen, "*Complexity Estimation. Building the intuition behind algorithm analysis*", http://www.atkinson.yorku.ca/~sychen/ITEC2620/ComplexityEstimation.pdf, pp.n/a, 2003

[CKM99] T.Culver, j.Keyser and D.Manocha, "*Accurate computation of the medial axis of a polyhedron*", Solid Modeling '99, pp.179-190, 1999

[DG03] T.Dey and S.Goswami, "*Tight Cocone: A Water-tight Surface Reconstructor*", Proceedings of the eighth ACM symposium on Solid modeling and applications, pp.127 - 134 , 2003

[DZ02] T.Dey and W.Zhao, "*Approximate medial axis as a Voronoi subcomplex*", Proceedings of the seventh ACM symposium on Solid modeling and applications, pp.356 - 366, 2002

[Geom] The Geometry Center , "*A Sample Geomview Data File*", http://www.geom.uiuc.edu/projects/visualization/hexbar-coords.html, pp.n/a, n/a

[GKS98] N.Gagvani, D.Kenchammana-Hosekote and D. Silver, "*Volume Animation Using the Skeleton Tree*", Proceedings of the IEEE Symposium on Volume Visualization, pp.n/a, 1998

[GLD03] open source, "*glData-OpenGL 3D data point viewer*", http://gldata.sourceforge.net/, pp.,

[GN00] M.Golin and H-S Na, "*On the average complexity of 3D-Voronoi diagrams of random points on convex polytopes*", Proc. of the 12th Annual Canadian Conference on Computational Geometry, pp.127-135, 2000

[GS98] N.Gagvani and D.Silver, "*Parameter controlled skeletons for 3D visualization* ", Proceedings IEEE Symposium on Volume Visualization, pp.n/a, 1998

[HAnim] Humanoid Animation Working Group of the WEB3D Consortium, "*The H-Anim 2001 specification*", http://h-anim.org/, pp., 2001

[Hil01] M.Hilaga et al, "*Topology matching for fully automatic similarity estimation of 3d shapes*", SIGGRAPH 2001 Conference proceedings, pp.203-212, 2001

[Hof90] C.Hoffman, "*How to construct the skeleton of CSG objects*", Proc. Fourth IMA Conf., The Mathematics of Surfaces, pp., 1990

[Hor95] C. Horiguchi, "*Sensors that detect shape*", Adv. Automation Technology, pp.210-216, 1995

[JB01] M.S.Jeong and B.Buxton, "*The affine skeleton of cross-sectional 3d human body scan data*", Preprint, University College of London, pp.n/a, 2001

[KTZ95] B.Kimia, A.Tannenbaum and S.Zucker, "*Shapes, shocks and deformations, I:The components of shape and the reaction-diffusion space*", International Journal of Computer Vision, pp.189-224, 1995

[LC87] W.Lorensen and H.Cline, "*Marching cubes: A high resolution 3D surface construction algorithm*", ACM/SIGGRAPH Computer Graphics, pp.163-169, 1987

[LCG03] L.Estrozi, L.Costa and P.Giblin, "*Affine Area Parallels and Symmetry Sets*", Preprint for submission to ICCV2003, pp.n/a, 2003

[LL92] F.Leymarie and M.Levin, "*Simulating the Grassfire Transform Using an Active Contour Model*", IEEE Transactions on Pattern Analysis and Machine Intelligence, pp.56-75, 1992

[LV99] F.Lazarus and A.Verroust, "*Level Set Diagrams of Polyhedral Objects*", Proceedings of the fifth ACM Symposium on Solid Modelling and Applications, pp.130-140, 1999

[MP02] M.Mortara and G.Patané, "*Affine-invariant skeleton of 3D shapes*", Proceedings of Shape Modeling International 2002, pp.245-278, 2002

[MP90] G.Martin and J.Pittman, "*Recognizing hand-printed letters and digits.*", Advances in neural information processing systems 2, Morgan Kaufmann Publishers Inc., pp.n/a, 1990

[MTT97] T. Möller and B.Trumbore, "*Fast, minimum storage ray-triangle intersection*", Journal of Graphics Tools, pp.21-28, 1997

[MWO03] W.C.Ma, F.C.Wu and M.Ouhyoung, "*Skeleton extraction of 3d objects with radial basic funcitons*", Proceedings of shape modeling international 2003 (to appear), pp.n/a, 2003

[NP85] L. Nackman and S. Pizer, "*Three-Dimensional Shape Description Using the Symmetric Axis Transform I:Theory*", IEEE Transactions on Pattern Analysis and Machine Intelligence, pp.187-202, 1985

[OB01] J.Oliveira and B.Buxton, "*Light weight virtual humans*", EUROGRAPHICS-UK,

pp.45-52, 2001

[Ogn92] R.Ogniewicz and M.Ilg., "*Voronoi Skeletons: Theory and Applications*", Proceedings of the IEEE Conference on Computer Vision and Pattern Recognition, pp.63-69, 1992

[Ogn93] Ogniewicz R.L, "*Discrete Voronoi Skeletons*", , pp., 1993

[Ogn95] R. Ogniewicz, "*Automatic Medial Axis Pruning by Mapping Characteristics of Boundaries Evolving Under the Euclidean Geometric Heat Flow onto Voronoi Skeletons*", Harvard Robotics Laboratory Technical Report, pp., 1995

[OJ03] J.Oliveira, "*Private communication*", n/a, pp.n/a, 2003

[Oli03] J.Oliveira et al., "*Animating scanned human models*", WSCG, Vol.11, No.1, pp.n/a, 2003

[PWH98] T.Poston , T.T. Wong and P.A.Heng, "*Multiresolution Isosurface Extraction with Adaptive Skeleton Climbing*", Computer Graphics Forum, pp.137-148, 1998

[Ree46] G.Reeb, "*Sur les points singuliers d'une forme de Pfaff completement integrable ou d'une fonction numerique*", Comptes Rendus Acad. Science Paris, pp.847-849, 1946

[SB98] D.Shaked and A. Bruckstein, "*Pruning Medial Axes*", Computer Vision and Image Understanding, pp.156-169, 1998

[Sch89] M. Schmitt, "*Some examples of algorithms in computational geometry by means of mathematical morphological techniques*", Lecture Notes in Computer Science, Geometry and Robotics, pp.225-246, 1989

[SE03] P.Schneider and D.Eberly, "*Geometric Tools for Computer Graphics*", Morgan Kaufmann, www.magic-software.com , pp.n/a, 2003

[SG98] P.Giblin and G.Sapiro, "*Affine invariant distances, envelopes and symmetry sets*", Geom. Ded. 71, pp.237-261, 1998

[SGIInv] SGI, "*SGI Inventor file format*", http://netghost.narod.ru/gff/graphics/summary/sgiinv.htm, pp.n/a, n/a

[She96] D.Sheeny et al, "*Shape Description by Medial Axis Construction*", IEEE Transactions on Vizualisation anc Computer Graphics, pp.62-72, 1996

[Sid99] K. Siddiqi et al., "*The Hamilton-Jacobi Skeleton*", International Conference on Computer Vision , pp.828-834, 1999

[SK96] K. Siddiqi and B. Kimia, "*Toward a Shock Grammar for Recognition*", EEE Conf. on Computer Vision and Pattern Recognition, pp.n/a, 1996

[SPB96] E. C. Sherbrooke, N. Patrikalakis, and E. Brisson, "*An algorithm for the medial axis transform of 3d polyhedral solids*", IEEE Transactions on Visualization and Computer Graphics, pp.44-61, 1996

[Su03] H. Sundar et al, "*Skeleton Based Shape Matching and Retrieval*", Proceedings, Shape Modelling and Applications Conference, SMI , pp.n/a, 2003

[Teic98] M.Teichman and S.Teller, "*Assisted Articulation of Closed Polygonal Models*", Proc. 9th Eurographics Workshop on Animation and Simulation, pp., 1998

[Wan01] M.Wang et al, "*Distance-field based skeletons for virtual navigation*", IEEE Proceedings of the conference on Visualization 2001, pp., 2001

[WDK01] M.Wan, F.Dachille and A. Kaufman, "*Distance-Field-Based Skeletons for Virtual Navigation*", Proceedings of the 12th IEEE Visualization Conference, pp.n/a, 2001

[Wil99] S. Wilmarth et al, "*Motion Planning for rigid body using random networks on the medial axis of the free space*", ACM Symp. on Computational Geometry, pp., 1999

[WOL92] F. Wolter, "*Cut Locus and Medial Axis in Global Shape Interrogation and Representation*", MIT Sea grant report, pp., 1992

[WP02] L.Wade and R.E. Parent, "*Automated Generation of Control Skeletons for Use in Animation*", The Visual Computer, pp.97-110, 2002

[Wu03] F.C. Wu et al, "*Skeleton extraction of 3d objects with visible repulsive force*", Eurographics Symposium on Geometry processing (2003), pp.n/a, 2003

[ZH81] S. W. Zucker and R. A. Hummel, "*A Three- Dimensional Edge Operator*", IEEE Transactions on Pattern Analysis and Machine Intelligence, PAMI, pp.324-331, 1981

[ZT99] Y.Zhou and A.Toga, "*Efficient Skeletonization of Volumetric Objects*", IEEE Transactions on Visualization and Computer Graphics, pp.195-206, 1999

APPENDIX A

PLANNING AND EXECUTION OF THE RESEARCH

The main aim of this research was to study the effects and properties of the 3d affine invariant skeleton in a variety of 3d objects but more importantly on 3d models of the human body. I therefore had to study the available algorithm in the literature, build the software to carry out the skeletonisation based on this algorithm, experiment on different object and human body scans and critically evaluate the results of my experiments and the properties of this algorithm.

I begun this project by creating a detailed waterfall-type plan, that would help me to organise my resources, time and effort appropriately. I come from a software engineering background, and I am used to creating such procedural plans when I need to build a software project. This however, was a different kind of project, a research project, and therefore I was sure how to approach it and whether or not my usual methods would suffice. After consultation with my project supervisor, I had a better idea on how to proceed and what where the major tasks I had to complete throughout the duration of this project.

My original plan, which was a Gannt chart, contained the following major tasks. Research into various popular skeletonisation methodologies, followed by detailed study of the theory and algorithm of the 3d affine invariant skeleton. The next task was to use this algorithm and build a working prototype of a program that could be used to compute the skeleton of primitive 3d models. Once both myself and my supervisor where happy with the preliminary results, I could move on to finalising the software and improving so that it could work with more complex object, and thus compute the skeleton of human body scans (which are topologically complicated). The next stage was verifying that the implemented program was stable and without any major errors. When I was confident that it was stable and working properly, it was time to move on to experimenting on complicated 3d ob-

jects. The final tasks was the writing of this dissertation, with a contingency time of approximately 2 weeks.

I therefore started with the most important stage, which was background literature research into the general areas of skeletonisation. This was a time consuming process considering that I did not know much about this specific research area. Sooner than later, I realised that I was slightly falling behind my original schedule. I overcame this problem by going back and slightly adjusting the durations of the any subsequent tasks. I also had to use up some of my planned contingency time.

Throughout the duration of this project, I kept a detailed journal of all my thoughts on the theory, problems, solution and interesting topics I happened to come across. The reason for this was that I soon realised that when the time came to write up my dissertation I could draw upon these journal entries as a way of retracing my steps and thoughts. In addition, because the amount of new theory was too much to handle in such a limited period of time, I wanted to use it as a repository and keep everything in a convenient place.

As my project moved on into the software development stage, I realised that the original waterfall type of plane that I had originally designed, did not suit my needs very well. I found myself, needing to go back and and revisit some previous stages, such as carrying out more literature research, when I could not understand how some parts of the algorithm worked. I therefore decided to chose a different type of plan, which allows a number of iterations between stages of the project. Since this is a research project, where sometimes even the question you are trying to answer and the path you have to follow may not be very well defined, a waterfall plan could not fully capture my needs. They are best suited for engineering tasks, where there is a linear path from task to task.

My new plan, allowed me to better organise my effort and resources, by iterating and completing more than on task in small intervals and in parallel. From there on, everything run smoothly on average an I managed to complete all our requirements in due time. Because of the way I planned my research, I had some extra time, that I used to introduce improvements to the original algorithm, that allowed my program to execute faster and more efficiently than the original algorithm stipulated.

Appendix A

Significance of the research

The most significant aspect of my research has been the use of the 3d affine invariant skeleton on models of the human body. So far, amongst its type of skeletons, only the medial axis has been used in body scans, which is not robust nor invariant under affine transformations, unlike other one-dimensional affine invariant skeletons.

As far as the skeletonisation algorithm is concerned, some improvements have been implemented and others introduced, that reduce the overall running time of the skeletonisation process and perhaps the overall quality of the end result.

As far as we know, this is the first time the 3d affine invariant skeleton has been subjected to such rigorous testing with a variety of data. We have established that, for 3d objects the affine skeleton will be a 2d surface in similar way to the 3d medial axis skeleton. We also proved by experiments that the fundamental properties of the affine skeleton, which are noise resistance and invariance under affine transformations, indeed extend to 3 dimensions. We have shown this, not simply by using an intuitive approach such as the way the skeleton looks, but based on detailed arithmetic calculations and comparisons.

This project was a continuation and extension to research previously undertaken in the computing department of UCL by M.S.Jeong and B.Buxton [JB01]. Their algorithm required manual intervention for segmentation and also requires that the human body was given in appropriate sliced format. We managed to build robust software, that can be used instead, with improved results, without manual intervention and more importantly able to work with more conventional formats [Geom] and data that is more similar to the one produced by the Body Lines 3d scanner available at the department.

APPENDIX B

B.1 The Zucker-Hummel gradient operator

The ZH gradient operator is a three-dimensional edge (surface detection) operator that incorporates information from a 3x3x3 adjacent voxels for a better approximation of the edge. The ZH operator is defined as:

$$G(x_{i,j,k}) = d_{(i+1,j,k)} - d_{(i-1,j,k)} +$$
$$k_1(d_{(i+1,j+1,k+1)} - d_{(i-1,j+1,k+1)} + d_{(i+1,j-1,k+1)} - d_{(i-1,j-1,k+1)} + d_{(i+1,j+1,k-1)} - d_{(i-1,j+1,k-1)} + d_{(i+1,j-1,k-1)} - d_{(i-1,j-1,k-1)}) +$$
$$k_2(d_{(i+1,j,k+1)} - d_{(i-1,j,k+1)} + d_{(i+1,j+1,k+1)} - d_{(i-1,j+1,k+1)} + d_{(i+1,j,k-1)} - d_{(i-1,j,k-1)} + d_{(i+1,j-1,k)} - d_{(i-1,j-1,k)})$$

$$G(y_{i,j,k}) = d_{(i,j+1,k)} - d_{(i,j-1,k)} +$$
$$k_1(d_{(i-1,j+1,k-1)} - d_{(i-1,j-1,k+1)} + d_{(i+1,j-1,k+1)} - d_{(i+1,j-1,k+1)} + d_{(i-1,j+1,k-1)} - d_{(i-1,j-1,k-1)} + d_{(i+1,j+1,k-1)} - d_{(i+1,j-1,k-1)}) +$$
$$k_2(d_{(i,j+1,k+1)} - d_{(i-1,j,k+1)} + d_{(i+1,j+1,k)} - d_{(i+1,j+1,k)} + d_{(i,+1j,k-1)} - d_{(i,j-1,k-1)} + d_{(i+1,j-1,k)} - d_{(i+1,j-1,k)})$$

$$G(z_{i,j,k}) = d_{(i,j,k+1)} - d_{(i,j,k-1)} +$$
$$k_1(d_{(i-1,j+1,k+1)} - d_{(i-1,j+1,k-1)} + d_{(i+1,j+1,k+1)} - d_{(i+1,j+1,k-1)} + d_{(i-1,j-1,k+1)} - d_{(i-1,j-1,k-1)} + d_{(i+1,j-1,k+1)} - d_{(i+1,j-1,k-1)}) +$$
$$k_2(d_{(i,j+1,k+1)} - d_{(i,j+1,k+1)} + d_{(i,j-1,k+1)} - d_{(i,j-1,k-1)} + d_{(i+1,j,k+1)} - d_{(i+1,j,k-1)} + d_{(i-1,j,k+1)} - d_{(i-1,j,k-1)})$$

where $k_1 = \frac{\sqrt{3}}{3}$ and $k_2 = \frac{\sqrt{2}}{2}$

B.2 3D Sobel gradient operator masks

Here are the 3x3 masks that can be used with a 3d Sobel operator, for gradient detection. The stacks are stacked in their respective direction to fill out a 3x3x3 cube.

-X direction: $$\frac{1}{32}\left\{\begin{bmatrix}1 & 2 & 1\\ 2 & 4 & 2\\ 1 & 2 & 1\end{bmatrix}_{x+1}\begin{bmatrix}0 & 0 & 0\\ 2 & 0 & 0\\ 0 & 0 & 0\end{bmatrix}_{x}\begin{bmatrix}-1 & -2 & -1\\ -2 & -4 & -2\\ -1 & -2 & -1\end{bmatrix}_{x-1}\right\}$$

-Y direction: $$\frac{1}{32}\left\{\begin{bmatrix}-1 & 0 & 1\\ -2 & 0 & 2\\ -1 & 0 & 1\end{bmatrix}_{y+1}\begin{bmatrix}-2 & 0 & 2\\ -4 & 0 & 4\\ -2 & 0 & 2\end{bmatrix}_{y}\begin{bmatrix}-1 & 0 & 1\\ -2 & 0 & 2\\ -1 & 0 & 1\end{bmatrix}_{y-1}\right\}$$

-Z direction: $$\frac{1}{32}\left\{\begin{bmatrix}1 & 2 & 1\\ 0 & 0 & 0\\ 1 & 2 & 1\end{bmatrix}_{z+1}\begin{bmatrix}2 & 4 & 0\\ 0 & 0 & 0\\ -2 & -4 & 0\end{bmatrix}_{z}\begin{bmatrix}1 & 2 & 1\\ 0 & 0 & 0\\ -1 & -2 & -1\end{bmatrix}_{z-1}\right\}$$

B.3 System and user manual

The source code contained with this project, is the main program and its supporting computational geometry libraries. The are written in C++ as nearly as possible in standard C++. We have included all the *.cpp class and *.h header files and a Makefile that when run should build the executable file. We tested this program on RedHat Linux 9.0 and the Makefile is tuned for such a system. It might be necessary to make a few alterations if it is ported on other platforms. We have successfully managed to build the program on a Sparc Solaris workstation, only by making some minor modifications such as including some standard C++ libriaries.

Once complied the program should be run as follows:

affine3d dT dD filename.off

Where *dT* is the discretisation size of the volumetric array, and *dD* the distance the cutting plane should travel. All values are calculated in pixels. *Filename.off* is the input file name in triangulated OFF format. The output of this program will be a file called “output.dat” containing the original vertices with their calculated erosion level-set function and their optimum normals. To erode or cal-

culate the skeleton it is necessary to uncomment the last part of the program, recompile and pass the “output.dat” file with the appropriate thresholds for erosion of skeletonisation.